Miniaturized Electron-impact-ionization Pumps using Double-gated Isolated Vertically Aligned Carbon Nanotube Arrays

By

Vivi Jayanty

B.S. Electrical Engineering and Computer Science
University of Washington, Seattle, 2007

Submitted to the Department of Electrical Engineering and Computer Science in Partial Fulfillment of the Requirement for the Degree of

Master of Science

at the

Massachusetts Institute of Technology

June 2012

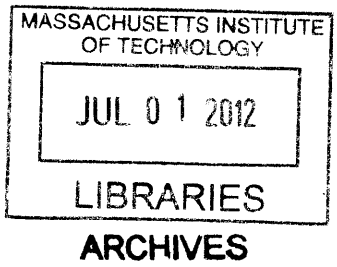

Signature of Author_____
Department of Electrical Engineering and Computer Science
February 29, 2012

Certified by_____
Luis Fernando Velásquez-García
Principal Research Scientist, Microsystems Technology Laboratories
Thesis Supervisor

Accepted by_____
Leslie Kolodziejski
Chairman, Department Committee on Graduate Students

Miniaturized Electron-impact-ionization Pumps using Double-gated Isolated Vertically Aligned Carbon Nanotube Arrays

By

Vivi Jayanty

Submitted to the Department of Electrical Engineering and Computer Science
On February 29, 2012 in Partial Fulfillment of the
Requirements for the Degree of Master of Science in
Electrical Engineering and Computer Science

Abstract

There is a need for microscale vacuum pumps that can be readily integrated with other MEMS and electronic components at the chip-scale level. Miniaturized ion pumps exhibit favorable scaling down because they are surface-limited and miniaturization increases the ratio between the active surface and the chamber volume, resulting in enhanced ionization and pump rates. Therefore, scaled-down ion pumps are a promising choice for a variety of applications including portable mass spectrometers and sub-mm wavelength vacuum amplifiers. Our micropump architecture consist of a field-emission electron source that is an array of double-gated isolated vertically aligned carbon nanotubes (VA-CNTs), an electron-impact-ionization region, and a non-evaporative ion-implantation getter.

Single-gated VA-CNT FEAs were tested as field emitters in high vacuum (10^{-9} Torr). The current density of the tested device is ~0.5A/cm^2 (total current of 0.4mA) and a field enhancement factor of 1.41×10^6 V/cm was measured, which is comparable to the simulation results by COMSOL. Two ways to fabricate double-gated VA-CNT FEAs were reported: one has the focus gate in plane with the extractor gate and the other has the focus gate above the extractor gate. Due to problems on fabrication process of double-gated VA-CNTs (short circuit between emitters, extractor gate, and focus gate), we were not able to collect four-terminal measurement, electron-impact-ionization, and pump data. However, procedure on how to collect and analyze field emission data with two gates to find β_G and β_F was described. In addition, procedures on how to collect and analyze data on electron impact ionization pump were also presented.

Thesis Supervisor: Luis Fernando Velásquez-García
Title: Principal Research Scientist, Microsystems Technology Laboratories

Acknowledgements

This work would not have been possible without the financial support of DARPA and the help, support, and guidance from a lot of people. First, I am especially thankful to my research supervisor, Dr. Luis F. Velasquez-Garcia, who has been supportive of my academic goals. He has provided me extensive personal and professional guidance and taught me a great deal about both scientific research and life in general. As my supervisor, he has taught me more than I could ever give him credit for here. He has shown me, by his example, what a good scientist could be.

I am also heartily thankful to Prof. Tayo Akinwande, whose encouragement, guidance, and support from the beginning enabled me to develop an understanding of the project.

I would like to take this opportunity to thank Dr. Wang Xiaozhi, whom I worked with for a short duration but I forged a special bond, for his encouragement and helpful advice. I owe my gratitude to Prof. Carol Livermore and Prof. Marty Schmidt and all DARPA micropump project members: Dr. Hanqing Li, Hui Zhou, Eric Newton, and Aalap Dighe for their feedback and advice to my research project. Thanks also go out to all MTL technicians and staffs for their help and valuable suggestions during my fabrication process over one and a half year.

I would especially like to thank Dr. Liang Yu Cheng. Her thesis provided a good foundation for me to start and extend this project.

I am also grateful to all of those with whom I have had pleasure to work during this project. I am indebted to many of my lab mates to support and guide me: Daniel Jang, Stephen Guerrera, Annie Wang, Melissa Alyson Smith, and Michael Swanwick. I would also like to show my gratitude to my best friend, Jack Dong, for his friendship, encouragement, and help.

At last, nobody has been more important to me in pursuit of this project than the members of my family. I would like to thank my parents, brother, and sisters, whose love and guidance are with me in whatever I pursue. They are the ultimate role models. Most importantly, I wish to thank my loving and supportive boyfriend, Jony Yuwono, who provides unending inspiration. Finally, I would like to take the opportunity to thank all my teachers.

Contents

List of Figures

List of Tables

1. Introduction and Motivation

The research on vacuum microelectronics has experienced a noticeable activity for over two decades while exploring the feasibility of a broad range of novel components and systems including sub-mm wavelength amplifiers, high-brilliance flat-panel displays, and portable analytical instrumentation [1]. Arguably, one of the most exciting trends in this effort is the miniaturization of systems that are portable and autonomous, i.e., with integrated support subsystems. Miniaturization of a system leads to compact size, lower power consumption, and lower cost [2]. These miniaturized systems typically operate at a pressure below standard atmospheric conditions, that is, they operate in vacuum. In some cases, the vacuum removes the constituents of the standard atmosphere that could cause an adverse physical or chemical effect on the system components during operation (e.g., mass spectrometry ionizers are very sensitive to oxygen and hence they benefit from an oxygen-free atmosphere). In other cases, a low-pressure atmosphere with a large enough mean free-path ensures that its constituent gas molecules do not interfere with the dynamics of the device (e.g., a particle accelerator needs vacuum to accomplish the acceleration of charged species in a pre-established trajectory with high reliability). Also, certain systems require control of the properties of the atmosphere (pressure, species composition, species energy distribution, etc.) to achieve a certain process in a repeatable manner (e.g. thin-film plasma etchers require a controlled environment that includes vacuum and continuous replenishment of the species that take part in the reaction to attain repeatability of the etch profile and etch rate).

In principle, two different vacuum systems that require dissimilar vacuum levels and mass flowrates cannot be satisfied using the same vacuum pump technology. For example, sputter coating and plasma etching commonly requires 0.05 - 1 Torr vacuum level while x-ray generators and mass spectrometers require $10^{-4} - 10^{-3}$ Torr to operate. Therefore, a number of pump technologies that are effective at setting and maintaining background atmospheres with certain specifications has been developed. In addition, parameters such as the reactivity of the gas mixture and the maximum operational pressure strongly influence the choice of the pump technology used to support these devices. Vacuum quality can be

divided into four levels: *low vacuum* (760 – 25 Torr), *medium vacuum* (25 – 10^{-3} Torr), *high vacuum* (10^{-3} – 10^{-9} Torr), and *ultra-high vacuum* (UHV: 10^{-9} – 10^{-12} Torr) [3]. Low vacuum (also called rough vacuum) is commonly used in applications that require a high gas flowrate, whereas high and ultra-high vacuum are mostly used in devices and processes that require very low gas flowrates and minimal interaction between the background gas and the devices.

In general, there are two kinds of vacuum pump technologies that can jointly span a wide range of flowrates and vacuum levels, i.e., vacuum pumps can be *mechanical*, where the vacuum is achieved by taking advantage of the compressibility of gases, or *non-mechanical*, where the vacuum is produced by exploiting other physical phenomena. Mechanical pumps have moving parts and conserve their pump capacity for long periods of time, while most non-mechanical pumps have a maximum capacity before regeneration. Examples of mechanical pumps are positive displacement pumps that create a vacuum by compressing pockets of gas using enclosed chambers with variable volume such as pistons and diaphragms [4], and turbo molecular pumps that create a vacuum by transferring momentum to the gas using high-speed rotating disks with blades [5]. Positive displacement pumps usually attain low vacuum, while turbo molecular pumps can reach high vacuum. Examples of non-mechanical pumps are as varied as the physical principles they exploit. For example, Knudsen pumps harness a thermodynamical phenomenon associated with rarefied gases between two gas reservoirs at different temperatures to create a vacuum with no moving parts [6]. Also, there are vacuum pumps based on the sublimation of Titanium that can attain ultra-high vacuum levels [7]. In addition, cryo pumps create vacuum by condensing the background gas on a cold surface while running thermodynamical refrigeration cycle [8].

Vacuum can also be created and maintained by ionizing the background atmosphere molecules and absorbing them into a solid. This is usually attained by striking plasma that ionizes the background gas and sputters an electrode (getter); the sputtered pieces react with the background gas, absorbing the gas molecules and hence creating vacuum [9]. Ion pumps are used in applications that require a contamination-free and vibration-free environment at ultra-high vacuum and with very low flowrate. Ion

pumps work better if scaled down because they are surface-limited (that is, the pumping occurs across a surface and the larger the surface, the larger the pumping capacity) and miniaturization of the ion pump results in larger surface-to-volume ratio (that is, more surface per unit of chamber volume results in faster pump rates). However, ion sputtering-based pumps are not attractive for many chip-scale systems because the pumping process generates a coating that can stick anywhere on the chamber and that could affect the performance of the system.

The main goal of MIT's chip scale micro vacuum pump project is to use MEMS technologies to create the technologies for miniaturized low-power vacuum pumps that can evacuate a small volume chamber from atmospheric pressure to high vacuum. Three vacuum pump stages that are used as can be seen in Figure 1: (i) a two-stage mechanical roughing pump that works with low vacuum from atmospheric pressure (760 Torr) down to low vacuum of tens of torr [10], (ii) a field ionization pump that works with medium vacuum, continuing the pumping from about 30 Torr to 1mTorr range, and (iii) the final stage is the field electron impact ionization pump that works with high vacuum from 10^{-3} Torr to 10^{-6} Torr.

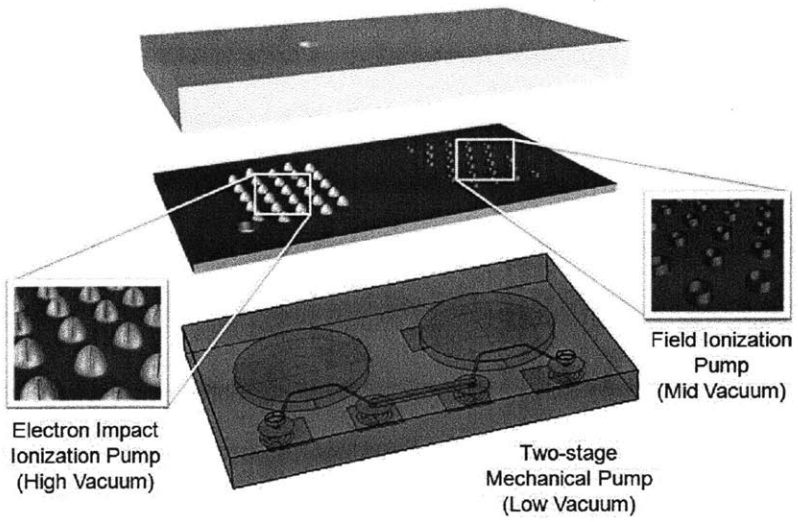

Figure 1: A schematic of MIT's chip scale micro vacuum pump, which consists of two-stage mechanical rough pump, field ionization pump for medium vacuum, and field emission electron impact ionization pump for high vacuum.

The goal of this thesis is to explore a micro-fabricated electron-impact-ionization-based ion pump architecture that does not sputter the getter and hence, it can support chip-scale systems that are very sensitive to contamination and/or that have very delicate components that are not compatible with sputtered coatings. The ion pump architecture is based on two physical principles: first, the ions are created by electron-impact-ionization using a field emission cathode [11] and second, the ions are implanted into the getter using a large acceleration potential [12]. Research on field emission electron impact ionizers using CNTs has been reported [13] because of their reliability and high field enhancement [14]. However, the ion pump architecture that we propose would make two key contributions to the state-of-the-art: (i) it will expand the working pressure range of ion pumps by using ion sources that are compatible with operation at pressures of 10^{-3} Torr or more and (ii) its use of a getter that is not sputtered will make the ion pump technology compatible with delicate vacuum systems that would be affected by the sputtered coatings. In addition, the micro-fabricated electron-impact-ionization pump that we report in this thesis can readily be integrated with other MEMS and electronic components at the chip-scale level, which should result in lower cost and better overall performance of the system.

2. Background

Electrons can be emitted from metal or semiconductor surfaces into vacuum through three distinctive processes: photoemission, thermionic emission, and field emission. In photoemission (Fig. 2a), electrons are emitted from a surface shined by photons if the photon energy is larger than the workfunction ϕ of the material. The number of emitted electrons depends on the intensity of the light beam. Photocathodes can produce ultra-short high-current pulses that are suitable for applications such as free electron lasers (FELs) [15] and they are insensitive to temperature fluctuations; however, photocathodes are very sensitive to contamination and humidity, and therefore, they require ultra-high vacuum to operate.

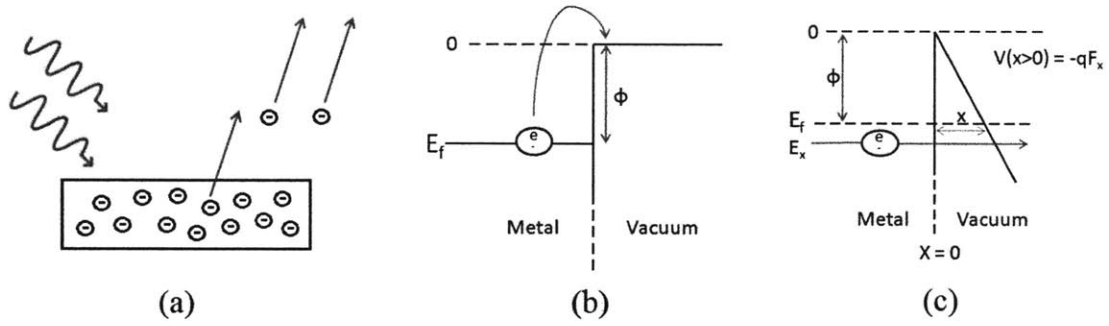

Figure 2: Three mechanisms of electron emission: (a) photoelectric emission, (b) thermionic emission, and (c) field emission.

In thermionic emission (Fig. 2b), electrons are boiled-off the emitting surface when the thermal energy of the electrons is large enough to overcome the barrier that confines them within the emitting material (workfunction ϕ) [16]. Thermionic cathodes are power hungry because they need to be heated at temperatures in excess of 1250K to emit electrons, and the majority of the power spent in heating the cathode is not transformed into power carried by the emitted current. A high-temperature surface is also very reactive; therefore, a vacuum of 10^{-5} Torr or more is required to operate a thermionic electron source. In addition, the thermal inertia of a thermionic cathode limits the bandwidth of the device; these delays are orders of magnitude larger than a typical delay due to the RC constant of the electronics that control the ionizer.

In field emission (Fig. 2c), electrons are emitted from metal and semiconductor surfaces into vacuum by applying locally a high electrostatic field that bends the vacuum level and reduces the barrier width [17]. If the energy barrier is narrow enough, electrons quantum tunnel out of the surface. The typical field emission triode is a sharp tip that is centered around an electrode aperture (gate) that faces a collector electrode (anode) as in Figure 3. The emitter is biased at a lower voltage with respect to the gate and the collector is typically biased at a higher voltage with respect to the gate. A sharp tip is used as emitter because it enhances the electric field on the tip surface. Field emitters can turn-on very fast, with switching speeds limited by the RC constant of the driving electronics. Also, since field emission is a quantum effect, the energy of the electrons does not need to be larger than the workfunction for the electrons to be emitted. Therefore, field emitters consume visibly less power than photocathodes and thermionic cathodes. In addition, field emitters can operate at orders of magnitude higher pressure, which makes them attractive for an electron-impact-ionization pump of a chip-scale system [18].

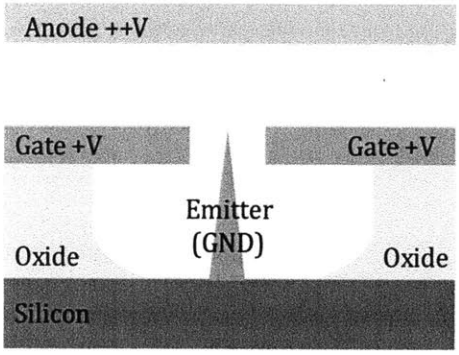

Figure 3: Single-gated field emitter triode.

2.1 Field Emission Electron Source

Field emission occurs when a high enough electrostatic field is applied on the surface of a metal or semiconductor, narrowing the width of the potential barrier to make electrons tunnel into vacuum. Field emission consists of a flux of carriers (i.e. supply function, $N(E_x)$ where E_x is the kinetic energy of the

electron along the emission direction x) and the transmission probability through the surface barrier (i.e. $D(E_x, F)$, where F is the electrostatic field on the surface). The current density $J(F)$ is given by

$$J(F) = \int N(E_x) D(E_x, F)\, dE_x \qquad (1)$$

where $N(E_x)$ depends on the x-velocity of the electron, the density of states, and the Fermi function. The transmission probability can be obtained by using Wentzel-Kramers-Brillouin (WKB) approximation [17]

$$D_{WKB}(E_x, F) = \exp\left[-2\sqrt{\frac{2m}{\hbar}} \int \sqrt{\left(\phi + E_f - E_x - qF\right)}\, dx\right] \qquad (2)$$

where ϕ is the workfunction of the tip material, m is the electron's effective mass, $\hbar = h/2\pi$ where h is Plank's constant, E_f is the Fermi level in the metal or semiconductor, q is the electron's charge, and x is the distance along the barrier width. After simplifications and approximations, Equation 1 results in the well-known Fowler-Nordheim (FN) equation, which relates the field-emitted current density to the electrostatic field at the surface [17]:

$$J(F) = \frac{A \cdot F^2}{1.1\phi} \cdot \exp\left[\frac{B(1.44\times10^{-7})}{\sqrt{\phi}}\right] \cdot \exp\left[-\frac{0.95B \cdot \phi^{\frac{3}{2}}}{F}\right] \qquad (3)$$

where $A = 1.56\times10^{-6}$ V.eV$^{-3/2}$ cm^{-1} and $B = 6.87\times10^{7}$ V.eV$^{-3/2}$ cm^{-1}. In a field emitter diode, the surface electric field F is related to the gate voltage V_G through $F = \beta \cdot V_G$, where β is the emitter field factor. The field factor β is to first order equal to the inverse of the tip radius r; therefore, emitters with very small tip diameter have associated a large field factor, resulting in field emission at low voltage. The emission current for a field emitter with one proximal gate that has an effective emission area a_{tip} is then

$$I(V_G) = \frac{a_{tip} \cdot A}{1.1\phi} \cdot (\beta V_G)^2 \cdot \exp\left[\frac{B(1.44\times10^{-7})}{\sqrt{\phi}}\right] \cdot \exp\left[-\frac{0.95B \cdot \phi^{\frac{3}{2}}}{\beta V_G}\right] \qquad (4)$$

Equation 4 can be rewritten as [19]

$$I(V_G) = a_{FN} \cdot V_G^2 \cdot \exp\left[-\frac{b_{FN}}{V_G}\right] \qquad (5)$$

with

$$a_{FN} = \frac{\alpha_{tip} A \beta^2}{1.1\phi} \cdot \exp\left[\frac{B(1.44\times10^{-7})}{\sqrt{\phi}}\right] \quad (6)$$

$$b_{FN} = \frac{0.95 B \phi^{\frac{3}{2}}}{\beta} \quad (7)$$

Electrostatics obeys linear superposition; therefore, a field emitter with two proximal gates will have an electrostatic field F on its tip equal to the linear superposition of the electric fields due to the two bias voltages. The structure of a field emission tetrode is a sharp tip that is centered around an extractor gate and a focus gate that faces a collector electrode (anode) as in Figure 4. The field at the tip surface of a double-gated field emitter depends on V_G, i.e., the bias voltage between the emitter and the extraction gate, and V_F, i.e., the bias voltage between the emitter and the focus, through the gate field factor β_G and the focus field factor β_F, respectively. Therefore, $F = \beta_G V_G + \beta_F V_F$ and Equation 4 becomes

$$I_{TIP} = \frac{\alpha_{tip} \cdot A}{1.1\phi} \cdot (\beta_G V_{G+} \beta_F V_F)^2 \cdot \exp\left[\frac{B(1.44\times10^{-7})}{\sqrt{\phi}}\right] \cdot \exp\left[-\frac{0.95B \cdot \phi^{\frac{3}{2}}}{\beta_G V_{G+} \beta_F V_F}\right] \quad (8)$$

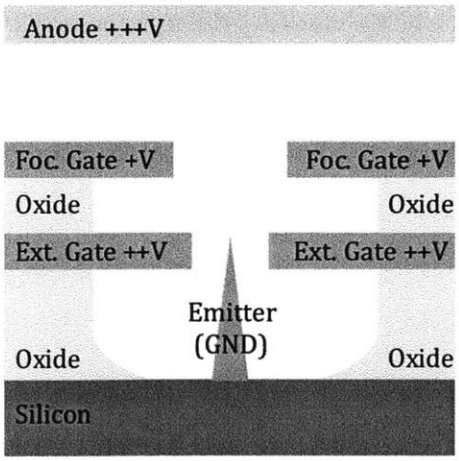

Figure 4: Double-gated field emitter tetrode.

A good field emitter array (FEA) design should provide proximal gates with individual electrode apertures that are concentric to each emitter to avoid electric field shadowing between neighboring field enhancers and off-axis emission. If the FEA is used for ionization, the presence of a second gate protects the field emitters from back ion bombardment; the second gate can also be used to collimate the beam in applications such as displays [20].

2.2 Electron Impact Ionization Pump

In the electron impact ionization process, a stream of electrons is accelerated to an energy several times higher than the gas molecules' ionization energy; ionization takes place when these energetic electrons collide with the molecules of the background gas and fragment them into charged pieces. An electron impact ionizer (EII) produces an ionization current I_i that is proportional to the electron current I_e, the number of density of neutral gas molecules ρ ($\rho = \frac{P}{K_b T} = \frac{N}{Vol}$, where P is the gas pressure, K_b is Boltzmann's constant, T is the temperature of the gas, and N is the number of gas molecules in a volume Vol), the length of the ionization region L, and the total ionization cross section σ_{Total} [21]:

$$I_i = I_e \cdot \frac{P}{K_b T} \cdot L \cdot \sigma_{Total}(E) = I_e \cdot \frac{N}{Vol} L \cdot \sigma_{Total}(E) \qquad (9)$$

Equation 9 shows that the ionization efficiency (i.e., ratio of ion current to electron current) is proportional to the background pressure and therefore, EIIs are more efficient at higher pressures. The electron source of the EII can be a photocathode, thermionic cathode, or a field emission cathode. In this project, we are using as cathode a double-gated FEA that uses isolated PECVD CNTs as field emitters because these cathodes have all the benefits of field emission-based electron sources that we previously pointed out and; in addition, CNTs are high aspect-ratio whisker-like structures with nanosized diameters that are very resilient, resulting in cathodes that can emit electrons at low (<100 V) voltage and that are capable of operating at high pressure, even in the presence of oxygen [22].

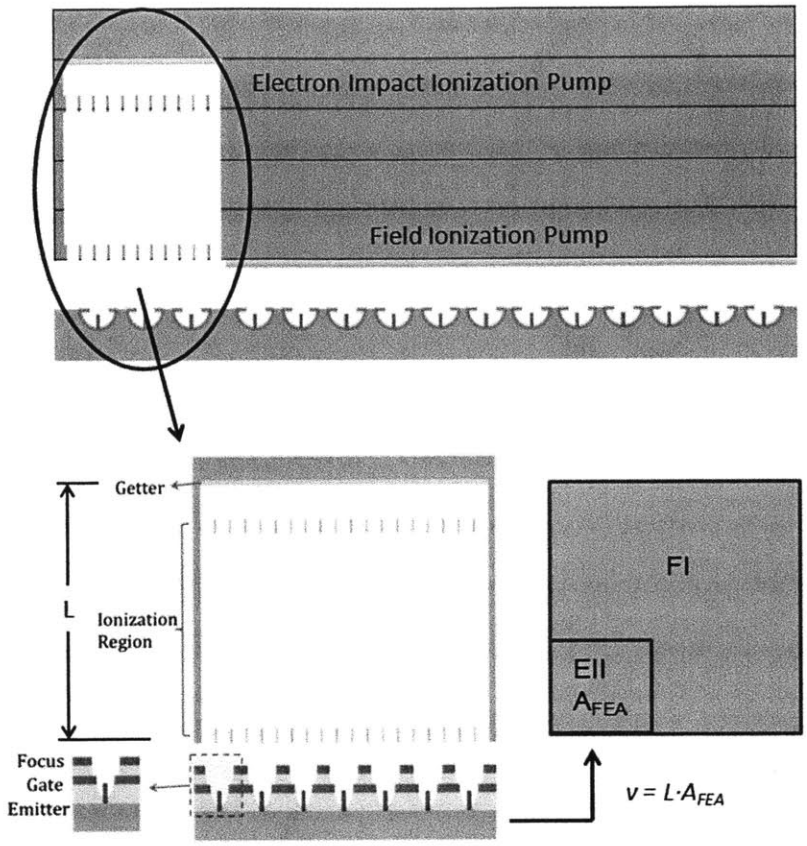

Figure 5: Schematic of field emission electron impact ionization pump. *Vol* is the total volume of electron impact ionization pump plus field ionization pump.

An EII can be used as part of an ion pump (Figure 5). In this scheme, the background gas is ionized by the EII and implanted into an electrode biased at high negative voltage (getter). The active volume of the ion pump v is smaller (or equal to) than the total chamber volume *Vol*. Therefore, we can assume that *Vol* is ξ-times the ionization volume v with $\xi \geq 1$. In this model, the ionization volume is equal to the active area of the FEA (A_{FEA}) times the ionization region L:

$$Vol = \xi \cdot L \cdot A_{FEA} \tag{10}$$

The total ionization cross-section is a measure of the probability that a given ionization process will occur when a molecule interacts with an electron. In Equation 9, it is implied that the ionization region is at a

constant potential so that σ_{Total} has a constant value. This is accurate if the ionization region is enclosed in high-transparency electrodes at the same potential.

The following pump model is based on the assumption that all the molecules that are ionized are implanted into the getter (no charge recombination, no neutralization). Implanting the ions into the getter reduces the number of molecules inside the chamber, which means that the system is creating vacuum. Based on the ideal gas law, the rate of change of pressure inside the chamber is proportional to the rate of change of the number of molecules inside the chamber:

$$\frac{dP}{dt} = K_b \cdot T \cdot \langle \frac{dN}{dt} \rangle_{Constant\ Volume} \tag{11}$$

where the rate of change of the number of molecules inside the chamber volume *Vol* is equal to the ion current per unit of charge (we assume that the ions are single-ionized) minus the leak rate $\dot{N}_{lk}$.

$$\frac{dN}{dt} = \dot{N}_{lk} - \frac{I_i}{q} = \dot{N}_{lk} - \frac{N(t)}{\tau} \tag{12}$$

where N is the number of molecules in the chamber at a given time and τ is a characteristic time

$$\tau = \frac{\xi \cdot q}{J_e \cdot \sigma_{Total}} \tag{13}$$

where J_e is the electron current density. In this model, we take into account two leak sources: (i) leak paths connected with the exterior that deliver a flowrate Q at standard conditions, and (ii) virtual leaks. The virtual leaks are, to first order, the outgassing of the internal surfaces of the vacuum chamber and they control the ultimate pressure and background atmosphere composition in high and ultra-high vacuum systems [23, 24]. Therefore, $\dot{N}_{lk}$ can be estimated as

$$\dot{N}_{lk} = \frac{Q \cdot P_{atm} + O_r \cdot A_s}{K_b \cdot T} \tag{14}$$

where O_r is the outgassing rate and A_s is the surface area of the vacuum chamber. Outgassing can be caused by (i) thermal desorption, (ii) desorption induced by electronic transitions, (iii) vaporization of materials, (iv) gas diffusion from the bulk and subsequent desorption, and (v) gas permeation through the walls.

By plugging in Equation 12 to Equation 11 and then integrating it, we find that the chamber ultimate pressure as a function of time is

$$P(t) = \left[P_o - \tau \cdot \dot{N}_{lk} \cdot K_b \cdot T\right] e^{-\frac{t}{\tau}} + \tau . \dot{N}_{lk} \cdot K_b \cdot T \qquad (15)$$

where P_o is the initial pressure inside the chamber. There are three possible situations of the pumping: (i) when the pump can overcome the leak, (ii) when the pump matches the leak, and (iii) when the pump cannot keep up with the leak. When the pump is faster than the leak rate, the ultimate vacuum generated by the pump (i.e., t >> τ) is equal to $P[t \to \infty] = \tau \cdot \dot{N}_{lk} \cdot K_b \cdot T$, assuming the getter is not exhausted. Therefore, in order to maximize the ultimate pressure, the characteristic time τ and the leak rate Q need to be as small as possible. The characteristic time τ can be minimized by increasing the volume (larger ξ) involved in pumping or increasing the emitter current density that means increasing the emitter current per tip, either by making the emitter tip sharper or the gate aperture smaller, or by having larger emitter density.

The second case is when the pump matches the leak. The pressure inside the chamber does not vary in time $P[t \to \infty] = P_o$. However, over time, the getter will get exhausted. On the other hand, when the leak can overcome the pump, the pressure inside the chamber increases and after a long period of time, the pressure will reach one atmosphere $P[t \to \infty] = P_{atm}$.

2.3 Objective and Technical Approach

The objective of this work is to explore a microscale vacuum ion pump architecture with non-evaporative ion-implantation getter that can be used to provide vacuum to other MEMS and electronic

components at the chip level. We propose to use an array of double-gated field emitters as electron source and ionize the background gas through electron-impact-ionization, then to implant the charged fragments into a solid getter using a high accelerating voltage. The goal of the research is to provide a proof-of-concept of the technology and determine the set of vacuum conditions (vacuum, leak rate) that it can satisfy.

2.4 Thesis Organization

The outline of the thesis is as follows:

Chapter 3 presents field emission electron impact ionization (FEEII) pump design, including field factor simulation and pump simulation.

Chapter 4 presents the fabrication for single- and double-gated VA CNTs FEA. The fabrication process to form the CNT nanodots, which is fast and repeatable, and to define the gate structure with two different techniques is discussed.

In chapter 5, the field emission measurement set up and IV characteristics with three-terminal and four-terminal measurements are presented along with comparison to the literature.

Chapter 6 presents the reason why our FEA did not work, the procedure on suggested ionization test set up and how to analyze the expected results.

Chapter 7 presents the procedure on suggested pump test set up and how to analyze the expected results.

Chapter 8 presents the summary of the thesis and suggestions for future work.

3. Device Design

The electron-impact-ionization pump that we report in this thesis consists of a double-gated FEA, an electron-impact-ionization region, and an ion-implantation getter. Isolated vertically aligned carbon nanotubes (VA-CNTs) are used as the field emission electron source because they are excellent field enhancers and they have good chemical and mechanical stability. The FEA has two proximal electrodes. A voltage applied between the inner electrode (extractor gate) and the emitters sets an electrostatic field on the tip of the emitters that results in electron emission. The outer electrode (focus) is biased at a voltage such that it attracts back-streaming positive ions, hence protecting the field emission tips. The pump works as follows: first, electrons are field emitted from the VA-CNT FEA; then, the electrons are accelerated in the ionization region using a bias voltage that maximizes the probability of collision with neutral gas molecules, this way achieving ionization of the background atmosphere molecules by fragmentation; finally, ions are implanted into a getter biased at a high negative voltage. A schematic of the pump process is shown in Figure 6.

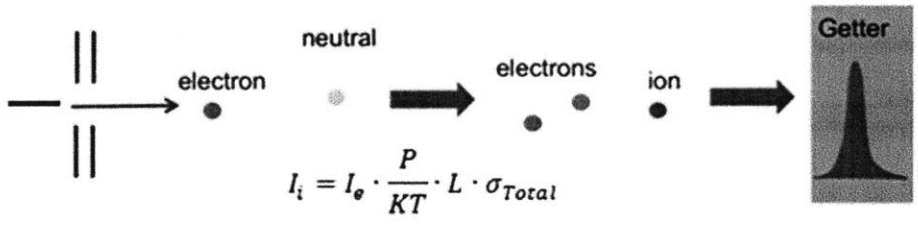

Figure 6: Schematic of field emission electron impact ionization pump process.

In order to explore the proposed ion pump architecture, design and simulation of double-gated VA-CNT FEAs were conducted to study how the position of the field emitter tip relative to the two gates affects the device performance (section 3.1). The dependence of the gate field factor (β_G) and the focus field factor (β_F) on the emitter tip size, emitter tip-to-electrode separation, and electrode aperture are explored using the commercial software COMSOL using the structure shown in Figure 7; these results quantify the effectiveness of the gate and focus electrodes to control the emission current. The VA-CNT

FEAs are designed to withstand high voltages (>150V), to maximize the electric field generated on the tips, and to minimize the electric field shielding effect from neighboring field emitters. The fabrication of the VA-CNT FEAs is described in chapter 4.

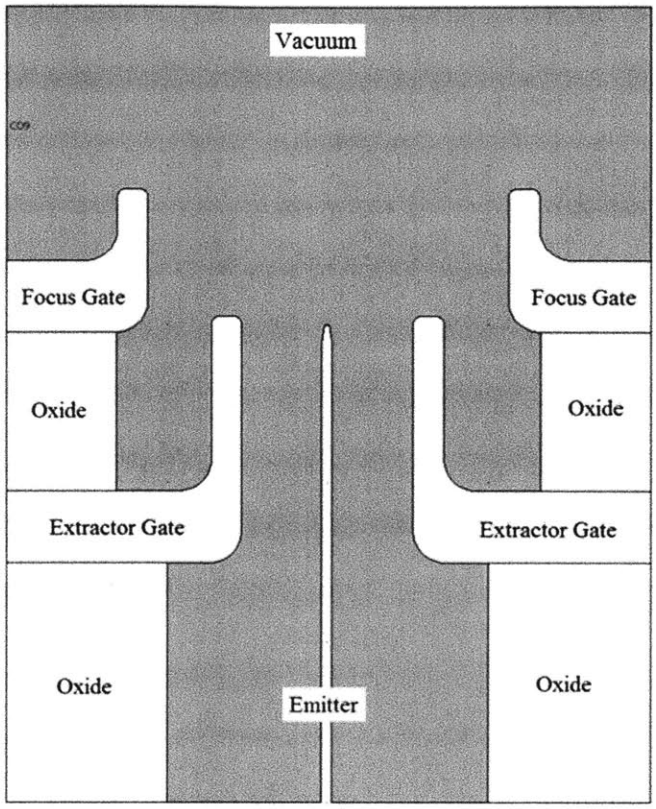

Figure 7: Schematic of an axis-symmetric double-gated field emitter (extractor and focus gates) to simulate the effective field factor of both gates.

3.1 Field Factor Simulation

The structure shown in Figure 7 is drawn in COMSOL to study how the tip emitter position with respect to extractor and focus gates affect the effective field factor of the field emitter. By specifying the boundary conditions (applying 1V to both extractor and focus gates and ground to the emitter), the structure is simulated to measure the effective field factor. The simulated electric field can be seen in Figure 8, with structure parameters as follows: the height of the emitter equal to 3μm, the emitter tip radius of 30nm, extractor gate aperture of 1μm, and focus gate aperture of 1.5μm. The maximum electric

field is generated at the tip, which is 9.16×10^5 V/cm for this case. It means that we need to apply ~33V to activate the field emitter (one needs about 3×10^7 V/cm to field emit electrons).

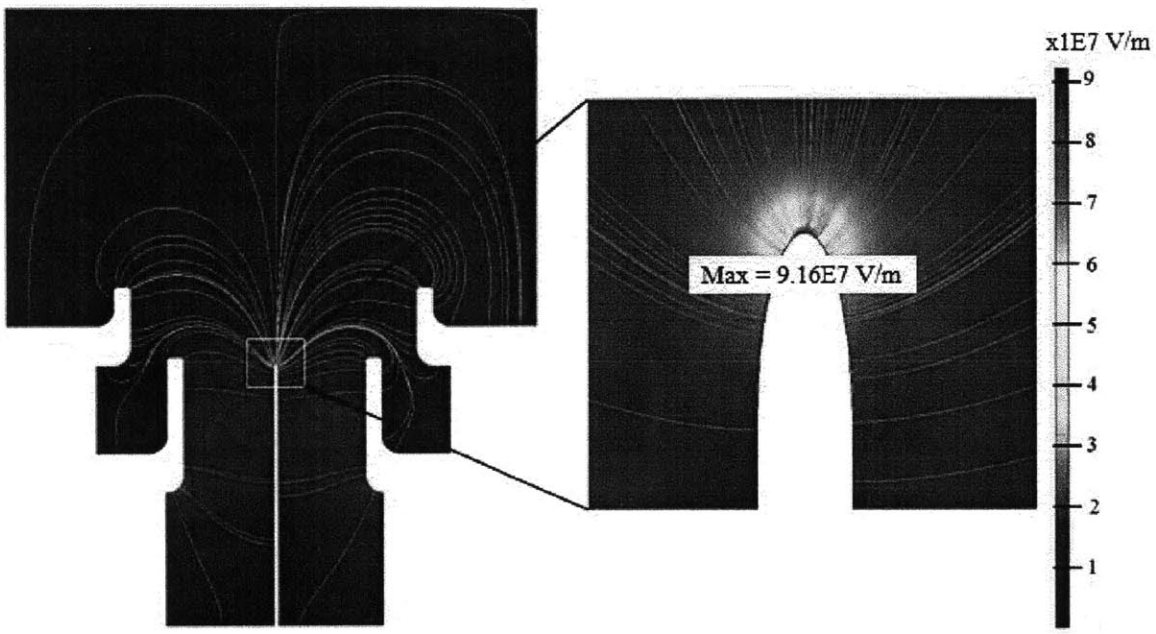

Figure 8: COMSOL simulation of the effective field factor (V/m) of a double-gated emitter with tip R = 30nm, extractor gate aperture = 1μm and focus gate aperture = 1.5μm. Both gates are biased at the same voltage (1V).

Using COMSOL, we explored different options by changing the tip radius (R), gate aperture (A_p), and tip position with respect to the extractor gate (h), as illustrated in Figure 9, to find the optimized structure of the field emitter.

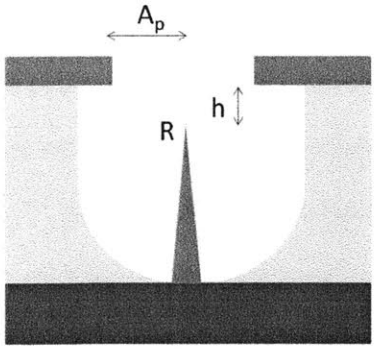

Figure 9 : Schematic of parameters varied in COMSOL simulation

The results for different parameters are presented in Figure 10, Figure 11, and Table 1. We found the relationship between field factor (β), gate aperture (A_p), and tip radius (r) from Figure 10 using the following equation:

$$\beta = C \cdot A_p^{\alpha} \cdot r^{B} \tag{15}$$

Using a least-square method, we calculated that C = $2x10^7$, α = -0.5, and B = -0.9 with C is in V·cm, A_p in μm, and r in nm. It shows that the effective field factor is inversely proportional to the extractor gate aperture to the power of 0.5 for various emitter tip radii. The further the gate from the tip (from 0.5μm to 1μm), the field factor decreases quite significantly. Therefore, the closer the tip to the gate (anode), the higher the enhancement factor is [25].

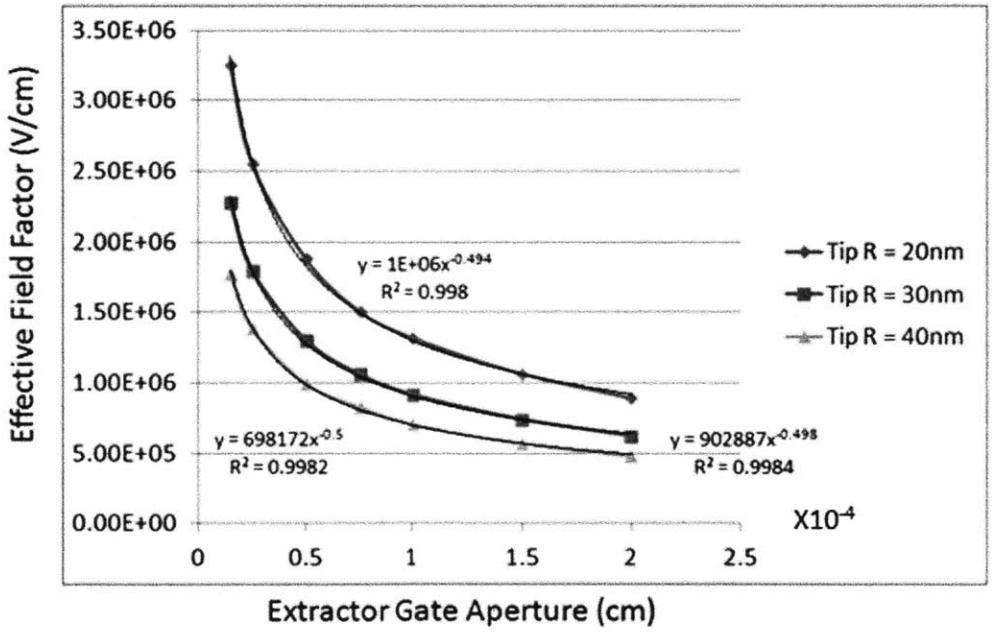

Figure 10: Effective field factor dependence on extractor gate aperture and emitter tip radius. The gate aperture is measured horizontally (in-plane) from the tip surface to the extractor gate. Both extractor and focus gates are biased at 1V.

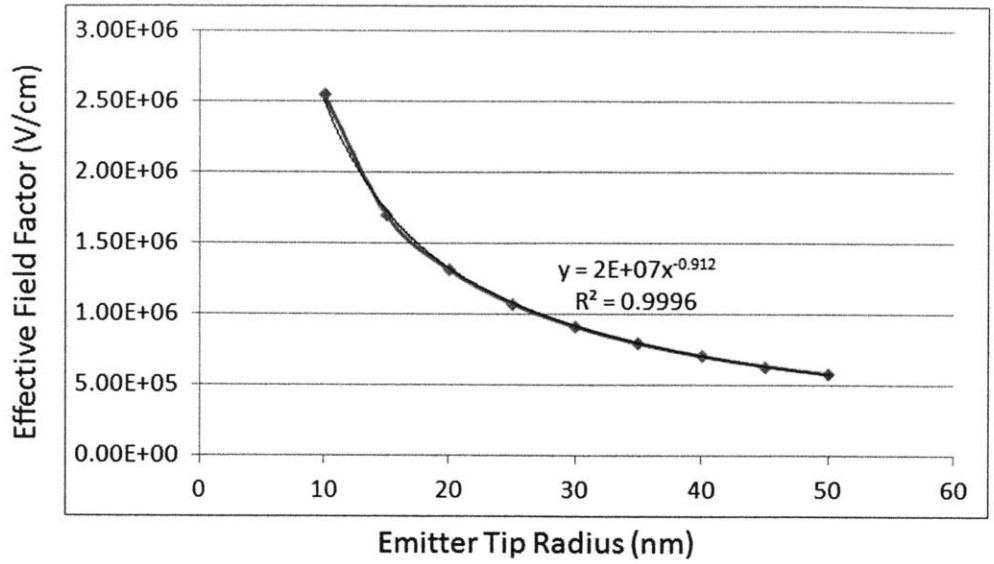

Figure 11: Effective field factor vs. Emitter tip radius simulated using COMSOL for gate aperture of 1μm with tip in-plane with the extractor gate. Both extractor and focus gates are biased at 1V.

Table 1: Effective field factor dependence on the emitter tip location with respect to the extractor gate for tip R = 30nm, extractor gate aperture = 1μm and tip R = 20nm, extractor gate aperture = 0.5μm. Focus and extractor gates are biased at the same voltage.

	Tip R = 30nm Gate Aperture = 1μm	Tip R = 20nm Gate Aperture = 0.5μm
Tip Position w/ respect to Extractor Gate	Effective Field Factor (V/m)	Effective Field Factor (V/m)
0.5μ below	8.61E+07	1.65E+08
0.3μm below	8.17E+07	1.49E+08
in-plane	9.16E+07	1.88E+08
0.3μm above	7.90E+07	1.25E+08
0.5μ above	7.58E+07	1.12E+08

As mentioned previously, the field factor at first order is inversely proportional to the emitter tip radius (with power of -0.91 and $R^2 > 0.99$), as presented in Figure 11. By plugging in A_p = 1μm to Equation 15, it is also confirms that the enhancement field factor is proportional to 1/r. In addition, D.L. Niemann's modeling also showed that emitter radius has the greatest influence on field enhancement factor of the CNT tip [26]. Table 1 shows that the best scenario for highest effective field factor is when

the emitter tip is in plane with the extractor gate, not below or above. Based on various simulation results, in order to maximize the effective field factor of the device, which means low turn-on voltage, requires a small emitter tip radius, a closer extractor gate aperture to the emitter tip, and an in-plane extractor gate with the emitter tip. However, for nano-size tips, the distribution of tip radii spread is large and skewed to the right (longer right tail) [27], which means that β widely varies across the array. Therefore, the goal would be to make emitters as sharp as possible to emit current at low voltage, but with near-monodisperse tip radii distribution. The optimized parameters that can be achieved to maximize the effective field factor; however, are also limited by the fabrication technique, which will be discussed in the chapter 4.

3.2 Pump Simulation

Pump performance is predicted using MATLAB under the condition presented in Table 2:

Table 2: Assumptions made in MATLAB to predict the pump performance.

Chamber Volume	20 mm^3
Initial Pressure	10-3 Torr
Pump Array Area	0.2 mm^2
Length of Ionization Region	3 mm
Current/tip	0.1 μA
Maximum Power	1 Watt
Chamber Outgassing Rate	$7.6x10^{-10}$ Torr.L/cm^2.sec

In these simulations, the field emission electron impact ionization pump starts working after the pressure in the chamber reaches 10^{-3} Torr. The pump array area needed is calculated based on the maximum power of 1Watt. As discussed in chapter 4, the ion pump described in this thesis is made of Silicon, amorphous Silicon (α-Si), CNTs, and silicon dioxide, and it is expected to operate at near-room temperature. Therefore, in this ion pump, the outgassing is mostly dominated by (i) desorption induced by electronic transitions, (ii) gas diffusion from the bulk and subsequent desorption, and (iii) gas permeation through the walls. A typical outgassing rate for a highly-polished metal surface such as the ones used in vacuum systems (polished stainless steel) is 7.6×10^{-10} Torr.Liters/cm^2.s [28]. The CMOS-grade thin films and substrates that we used in this process have lower outgassing rates than the outgassing rates of polished bulk metal because of the orders of magnitude smaller defects on the CMOS-grade materials and their order-of-magnitude smoother surfaces. Therefore, we expect outgassing rates smaller than what is quoted in the literature for vacuum-compatible metal parts. As a result, the leaking in the pump described in this thesis is mostly dominated by the volumetric leak rate Q.

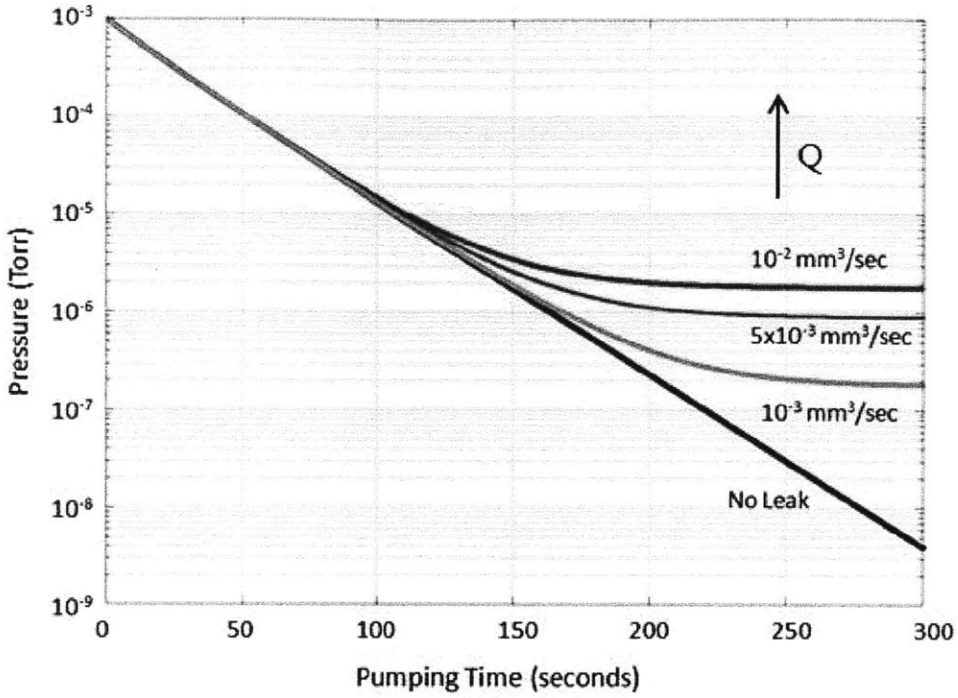

Figure 12: MATLAB simulation of the pumping performance of the Electron Impact Ionization pump for various leak rates (Q). The volumetric leak rate is three-orders of magnitude larger than the outgassing rate.

Figure 12 shows that the maximum leakage rate allowed in order for electron impact ionization pump to be able to reach 10^{-6} Torr is ~$5x10^{-3}$ mm^3/sec. The leak rate is mostly dominated by the volumetric leak rate (three-orders of magnitude larger than the outgassing rate).

There are also the cases when the leak rate is equal to the pump rate and when the leak rate is larger than the pump capacity. Figure 13 shows the simulation of both cases. When the leak rate is equal to the pump rate, which is ~$5mm^3$/s based on MATLAB simulation, the pressure stays at the initial chamber pressure. Meanwhile, when the pump capacity cannot keep up with the leak rate, the chamber pressure goes up to 1 atmosphere pressure after a period of time.

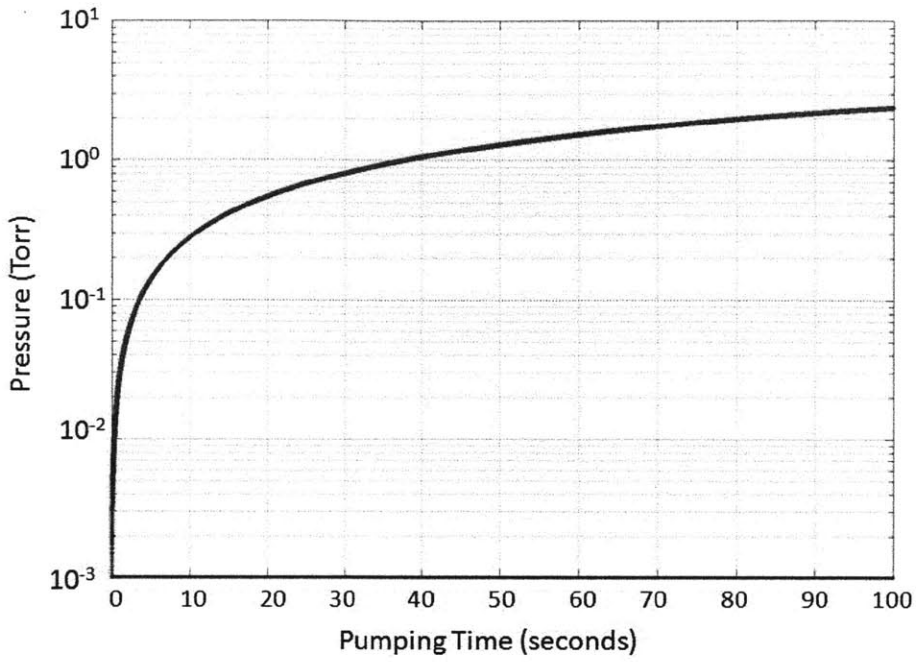

Figure 13: MATLAB simulation of pumping performance for Electron Impact Ionization pumps when the pump rate equal to the leak rate (blue line) and when the pump rate cannot keep up with the leak rate (green line). The leak rate is dominated by the volumetric leak rate.

4. Device Fabrication

4.1 Single-gated VA-CNTs FEA

The fabrication of the double-gated VA-CNT FEAs starts with the deposition of a 50 nm-thick sputtered TiN film and that is annealed at 800°C for 30 seconds in order to decrease the resistivity and increase the film density [29]; the fabrication continues with the deposition of a 20 nm-thick evaporated Ni film as shown in Figure 14 - step 1. Next, 600 nm-wide Ni/TiN pads with 5 μm pitch are defined using projection lithography, plasma etching, and wet etching (Figure 14 - step 2). The Ni is initially etched using plasma to define 600nm dots using a mixture of Cl_2/Ar [30] (recipe listed in Appendix A) and then, the Ni is etched using Ni etchant to further decrease the size of the dot to ~250nm to grow one CNT per Ni dot [31]. Next, plasma-enhanced chemical vapor deposited (PECVD) VA-CNTs are grown using the Ni pads as catalyst (Figure 14 - step 3). There are many factors that affect the growth of VA-CNTs including the catalyst material, the thickness of the catalyst, the size of the catalyst pad, the growth temperature, the growth time, the plasma bias voltage, and the composition and pressure of the gas mix during growth. To grow 3-4μm-tall vertical CNTs of high-quality, we routinely use Ni as catalyst and a 1:2 NH_3:C_2H_2 gas mix; we heat the substrate at 770°C and turn on the plasma for 20 minutes. A SEM picture of these vertically aligned CNTs is shown in Figure 15.

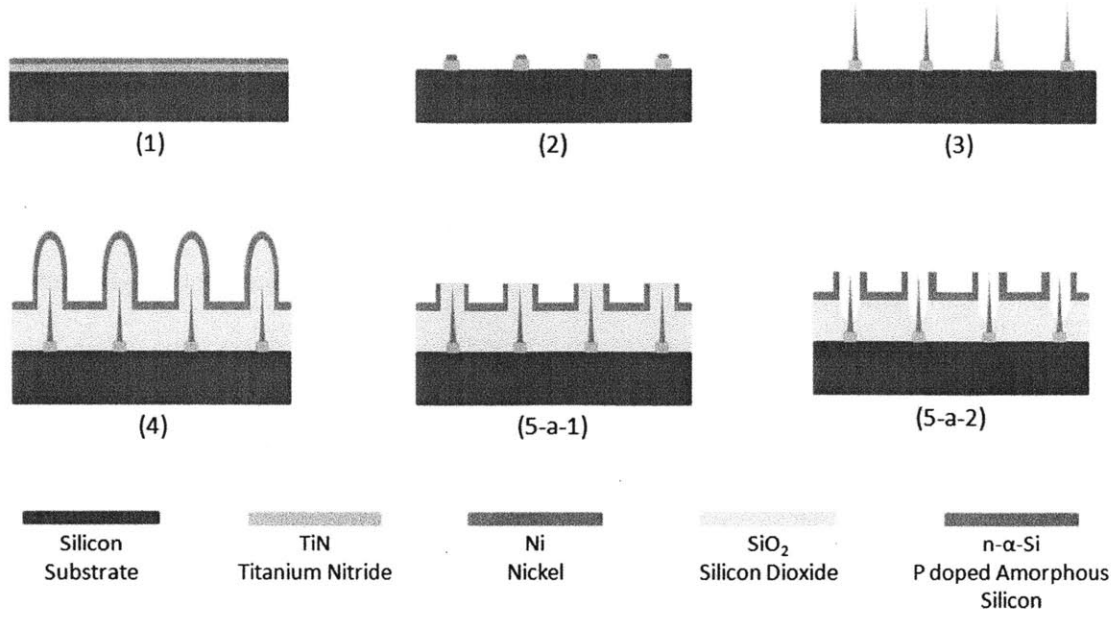

Figure 14: Process flow of single-gated VA CNTs.

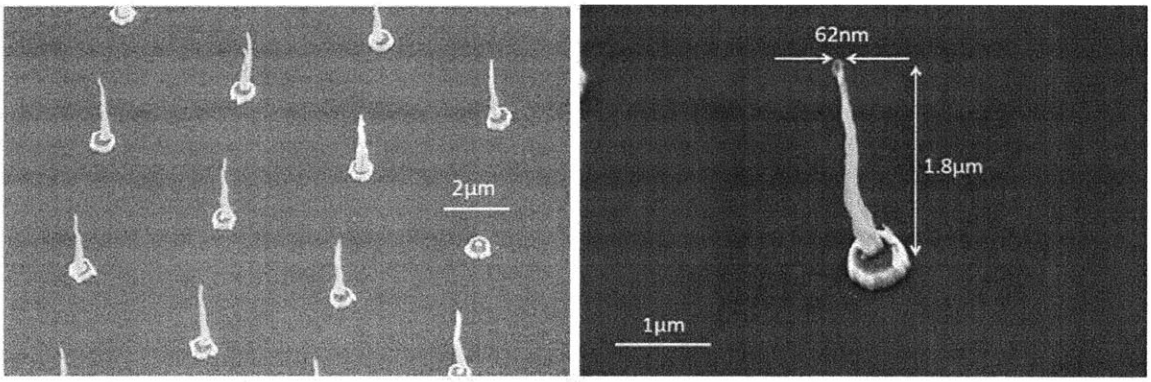

Figure 15: (a) Array of VA-CNTs 3-4μm tall. (b) An isolated VA-CNT with 3.6μm height and 62nm tip diameter. SEM was taken from 30 degree angle.

The fabrication continues by depositing a 1.5μm-thick conformal layer of PECVD oxide that will be used as insulator between the CNTs and the extractor gate. The thickness of the deposited oxide determines the gate aperture. Referring to Appendix C, the ratio of deposited horizontal oxide to vertical oxide is 4:3. Therefore, by depositing 1.5um oxide, the gate aperture is about ~1.1μm. In addition, a 1μm

of PECVD oxide can withstand ~500V before the breakdown [32]. However, a more reasonable value will be ~300V/μm, considering different deposition conditions. Therefore, 1.5μm of oxide thickness will be a safe choice of gate insulator to prevent breakdown during operation. Then, a conformal layer of 0.45 μm-thick PECVD doped α-Si film is deposited on top of the oxide to form a gate electrode later in the process (Figure 14 - step 4). The experimental result up to this process step can be seen in Figure 16.

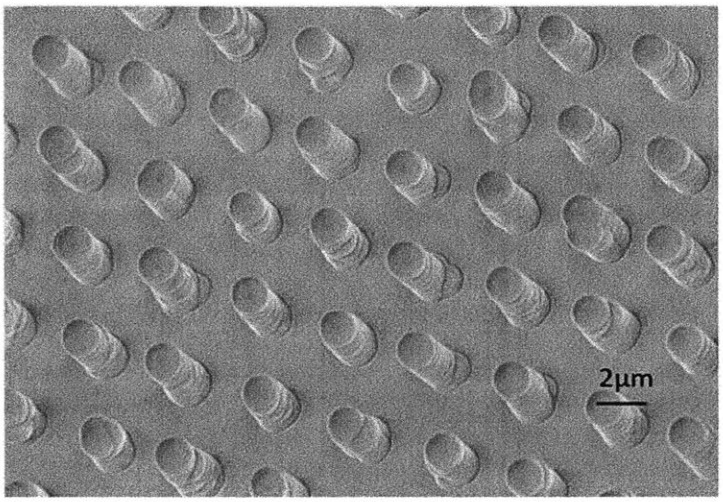

Figure 16: SEM of an array of CNTs deposited with oxide and n-amorphous-Si.

Next, contact lithography and plasma etching are used to pattern the α-Si to define the extractor electrode for the different FEAs (Figure 17). Single-gated FEAs can be constructed at this stage of the process flow if the emitter apertures are open (step 6-a-1 and 6-a-2 in Figure 14). The technique we use to open the apertures is CMP (Chemical Mechanical Polishing). This technique provides a method to define apertures that are self-aligned to the emitter tips. The position of the emitter tip relative to the extraction gate aperture depends on the polishing time. The samples need to be polished until the emitter tips are in plane with the gate aperture to maximize the electric field enhancement. Figure 18 shows the single-gated VA-CNT FEAs after releasing the oxide using BOE.

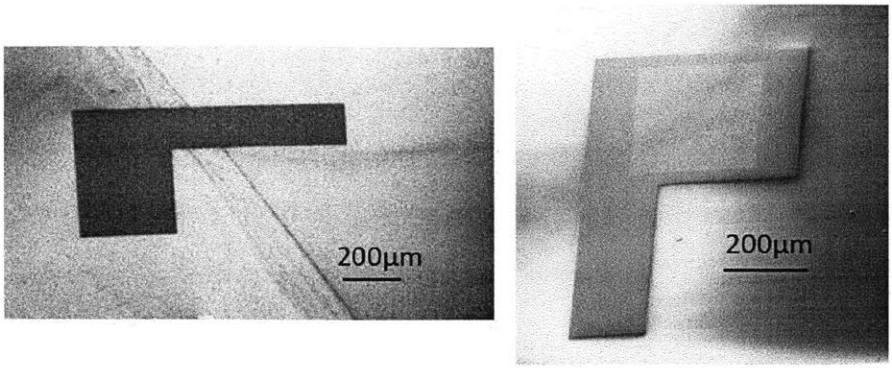

Figure 17: Extractor gate electrode. The left picture is electrode for 5x5 FE arrays and the right picture is for 200x200 FE arrays.

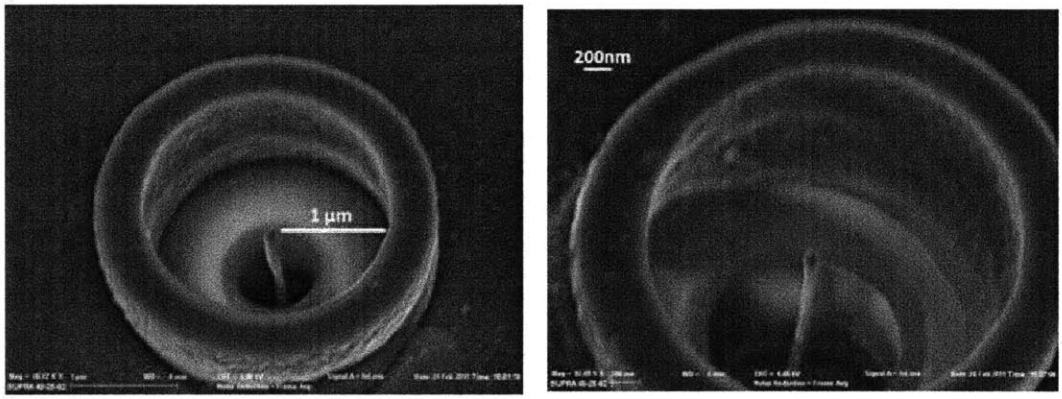

Figure 18: Single-gated VA-CNT FEAs.

4.2 Double-gated VA-CNTs FEA

4.2.1 Focus Gate in-plane with the Extractor gate

Double-gated VA-CNT FEAs with the focus gate in-plane to the extractor gate can be fabricated if instead of opening the extractor gate apertures using BOE, a conformal layer of 1µm-thick of PECVD oxide is deposited on top of the α-Si film right after being patterned using contact lithography; this oxide film is intended to insulate the focus gate from the extractor gate. A thickness of 1µm is chose with consideration of providing enough vertical distance between the extractor and focus gate and also the limitation of the total deposited film thickness (1.2µm oxide + 0.45µm α-Si + 1µm oxide + 0.45µm α-Si = 3.1µm) not exceeding the CNT height (3-4µm) as illustrated in Figure 19. If the CNT height H_{CNT} is

shorter than $H_{O1} + H_{O2} + 2$ α-Si thicknesses, the top α-Si layer got polished in order to get an in-plane structure during CMP process.

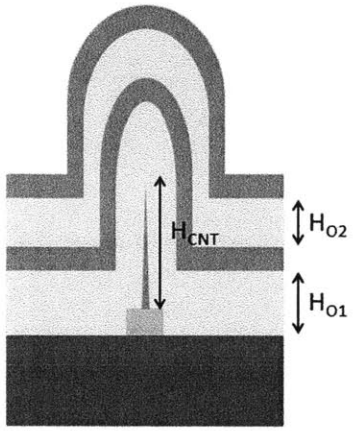

Figure 19: Illustration of CNT height compared to the thicknesses of deposited oxide and α-Si film.

Since a polishing technique is used to open both gates, in order to get a focus gate that is in-plane with the extractor gate, the deposited film thickness cannot go above the CNT tip or else it will polish the focus gate film material. Then, 0.45 μm-thick α-Si film is deposited on top of the second silicon dioxide film (Figure 20 - step 5-b-1) as base material to form the focus gate later in the process. Patterning of the focus gates of the different FEAs is conducted using contact lithography and plasma etching; after that, vias for the extractor electrodes are etched on the second silicon dioxide film using lithography and wet etch (Figure 21).

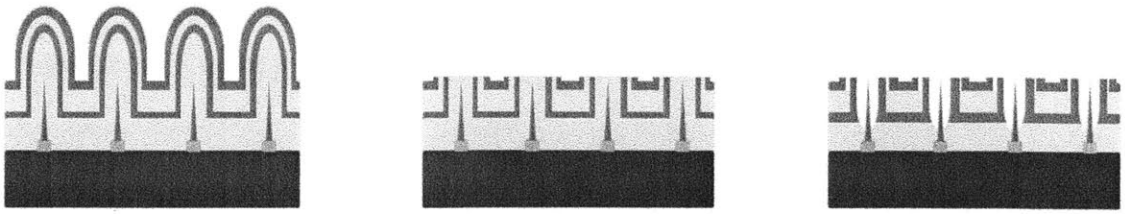

Figure 20: Process flow to fabricate double-gated VA-CNT FEAs with focus gate in-plane with the extractor gate.

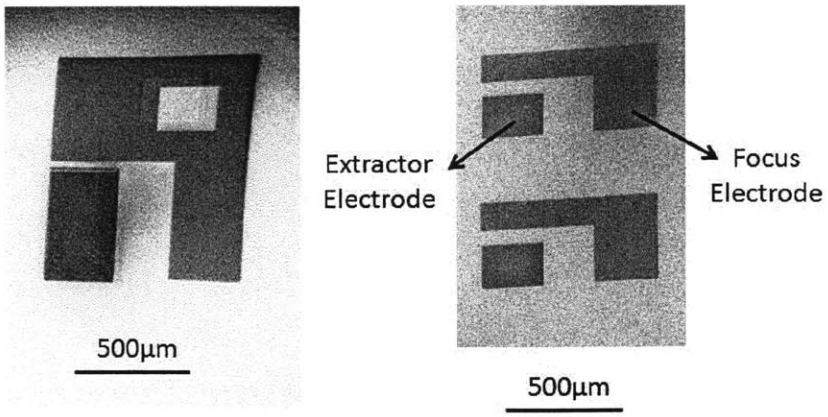

Figure 21: Extractor and focus gate electrodes, and via to the extractor gate electrode.

Next, the CMP technique described before is used to define the extractor gate and focus apertures (Figure 20 - step 5-b-2). The last step of the fabrication process flow is releasing the emitter tips using a BOE etch (Figure 20 - step 5-b-3). The result is in Figure 22.

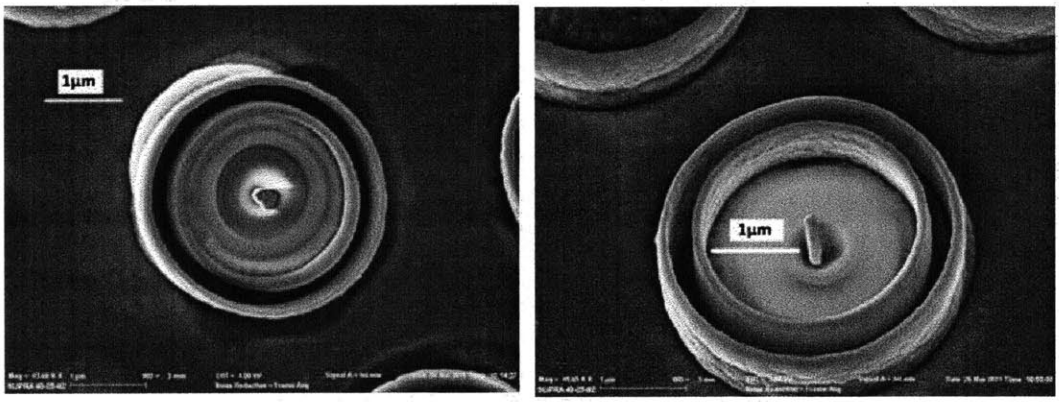

Figure 22: SEM of double-gated VA-CNT FEAs with focus gate in-plane with the extractor gate.

4.2.2 Focus Gate above the Extractor gate

The position of the focus gate with respect to the emitter tip does not affect the effective field factor significantly. However, the focus gate works more efficiently to protect the tip from ion bombardment during ionization, if the focus gate is located on top of the extractor gate, instead of in-plane. Double-gated VA-CNT FEAs can be fabricated with focus gate above the extractor gate by depositing a conformal layer of 0.8-1μm-thick of PECVD oxide on top of the α-Si film after being patterned using

contact lithography and planarization; this oxide film is intended to insulate the focus gate from the extractor gate. A thickness of 1μm was chosen to prevent breakdown. The thickness of the oxide can be less than 1μm because the voltage difference applied between extractor and focus gates does not exceed 30V to prevent electric field generated between the two gates. Then, 0.45 μm-thick α-Si film is deposited on top of the second silicon dioxide film (Figure 23 - step 5-c-1) as base material to form the focus gate later in the process.

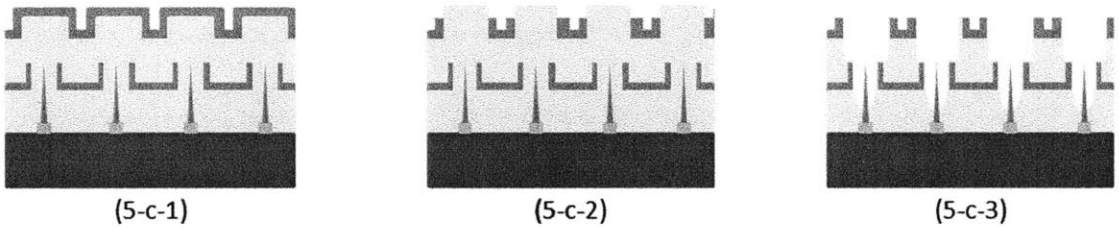

Figure 23: Process flow to fabricate double-gated VA-CNT FEAs with focus gate above the extractor gate.

Patterning of the focus gates of the different FEAs is conducted using contact lithography and plasma etching; after that, vias for the extractor electrodes are etched on the second silicon dioxide film using lithography and wet etch (Figure 21). Next, a photolithography (Figure 24) and plasma etching technique is used to define focus apertures (Figure 23 - step 5-c-2), which is different from the technique to open the extractor gate.

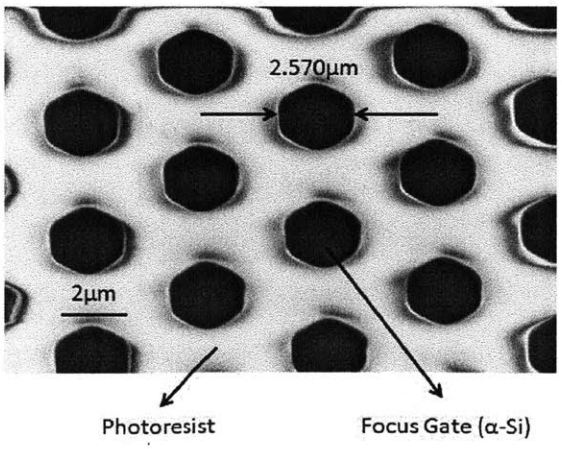

Figure 24: SEM of photolithography to define focus apertures.

The last step of the fabrication process flow is releasing the emitter tips using a BOE etch (Figure 23 - step 5-c-3). The process flow to fabricate double-gated CNT FEAs with focus gate above the extractor gate can be seen in Figure 23, followed by the SEM.

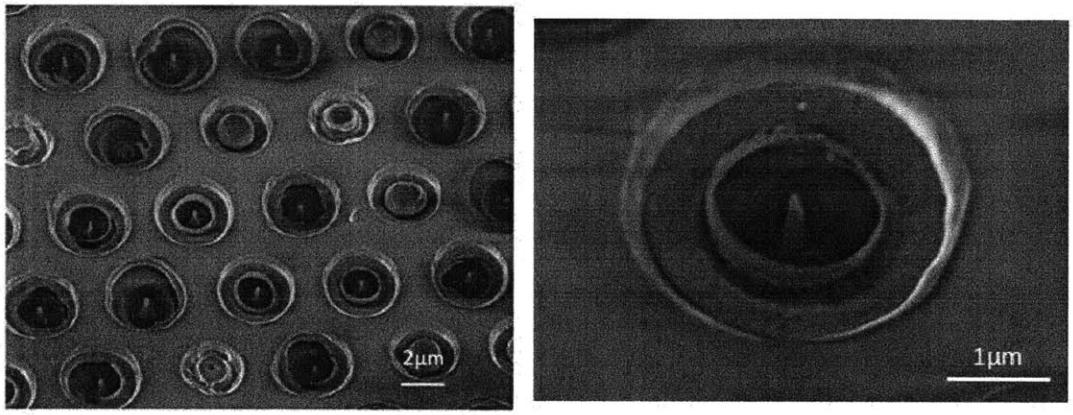

Figure 25: SEM of double-gated VA-CNT FEAs with focus gate above the extractor gate.

5. Field Electron Source Characterization

5.1 Field Emission Measurement Set up

A series of tests were conducted to benchmark the performance of the fabricated devices and compare it with the models and simulations. First, the FEAs were used as electron sources in ultra-high vacuum to conduct field emission tests as shown in Figure 26. A set of Keithley 237s controlled by Labview was used to bias voltages to the substrate (emitter tips), extractor gate, focus gate, and the anode ball (collector). The instrument has capability of measuring a maximum current of 10 mA and applying a voltage between -1100V and +1100V. The emitter is grounded while the gate voltage is varied between 0 to 200V. The collector, which is a 2 mm diameter metallic sphere hanging ~3mm above the tested device, is biased at +1100V for field emission tests. To show that the extractor gate current and the collector current comes from the same physical origin, the total emitted current should be equal to the current intercepted by the extractor gate plus the current collected by the anode ball and there should be a linear relationship among the emitted, intercepted, and collected currents. For field emission tests, the IV characteristics (Emitter, Gate, and Anode Currents vs. Emitter Voltage) were collected at a chamber pressure of $5x10^{-9}$ Torr. Based on the data, we estimated the extractor gate field factor β_G and focus gate field factor β_F. Using the commercial software COMSOL, we built a finite element model of the fabricated device using the dimensions obtained from its SEM metrology as discussed in section 3.1; the finite element results were then compared to the field factor estimated from the experimental data.

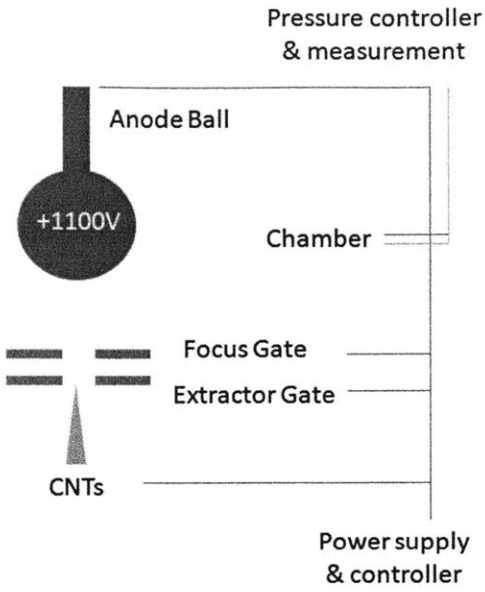

Figure 26: Field emission testing set-up to estimate the gate and focus field factors.

5.2 Three-terminal Measurements

The single-gated FEAs were successfully fabricated and field emission tests were conducted by biasing the anode at +1100V, the substrate/emitters (CNTs) at 0V, and by varying the extractor gate voltage from 0V to +200V in small increments (2V). Currents versus emitter voltage data were collected as shown in Figure 27. The size of the FEA tested is 100x100 with about 30-40% of the emitters working due to the non-uniformity of the CNT heights (determined from SEMs). A total emitted current of ~0.4mA was produced at an applied voltage of 200V. Assuming uniform operation of the FEA, the current emitted per tip is ~0.1μA. As a comparison, experiments by J.M. Bonard showed that an individual ~4nm tip radius multiwall carbon nanotubes are capable of stably emitting ~2μA when biased at 200V for more than 100 hours [33]. In addition, Guillorn et al reported 700nA field emission current at 90V using a gated individual carbon nanofiber (tip radius of 15nm and height of 1μm) with the collector anode (100V) located 700μm above the gate [34].

The data collected were analyzed to obtain a Fowler-Nordheim (FN) plot, i.e., $\ln(I/V^2)$ vs. 1/V, shown in Figure 29. The parallel straight line confirms good correlation with the FN model. In addition, the three

slopes (emitter, gate, and anode data) of the FN plots agree. The slope of the graph (emitter), i.e., b_{FN}, is calculated using the least-square method, which is 500.89. From equation 7, the field factor of the device β_G is calculated to be 1.35×10^6 [cm^{-1}]. Based on the β estimates from the COMSOL simulation shown in Figure 10, the simulated tip radius is ~20nm. It is comparable to the emitter tip radius observed under SEM, which is 25-30nm (Figure 30).

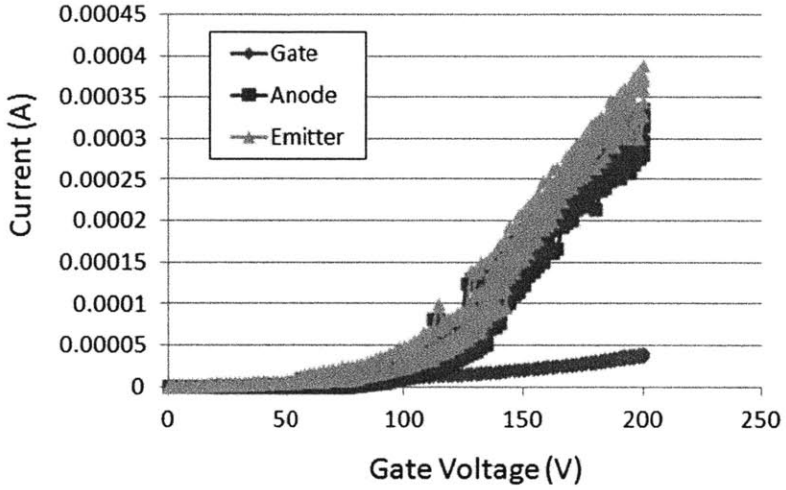

Figure 27: IV Characteristic Data for Three-terminal Field Emission Electron Source.

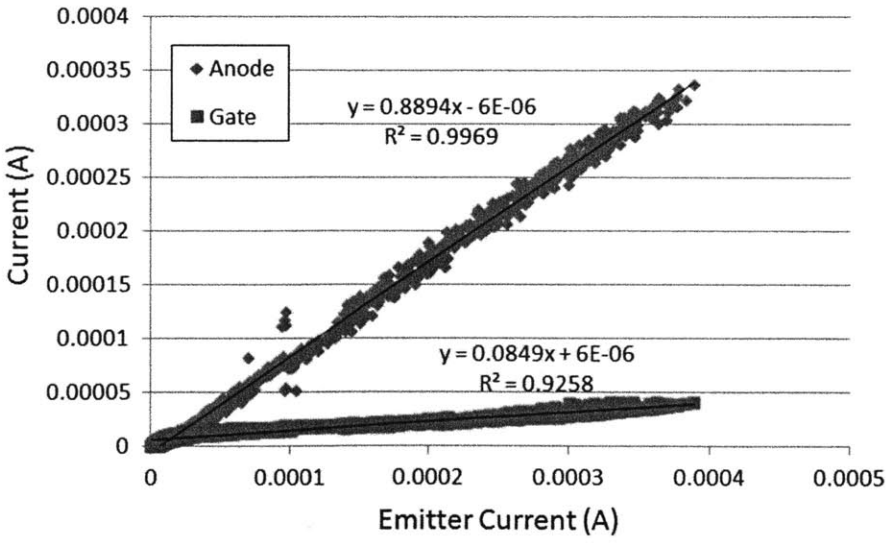

Figure 28: Emitter Current vs. Anode Current Plot.

A graph of anode and gate currents versus emitter current was plotted in Figure 28. From the plot, we infer that 89% of the emitter current was collected at the anode ball and only < 10% was intercepted in the extractor gate.

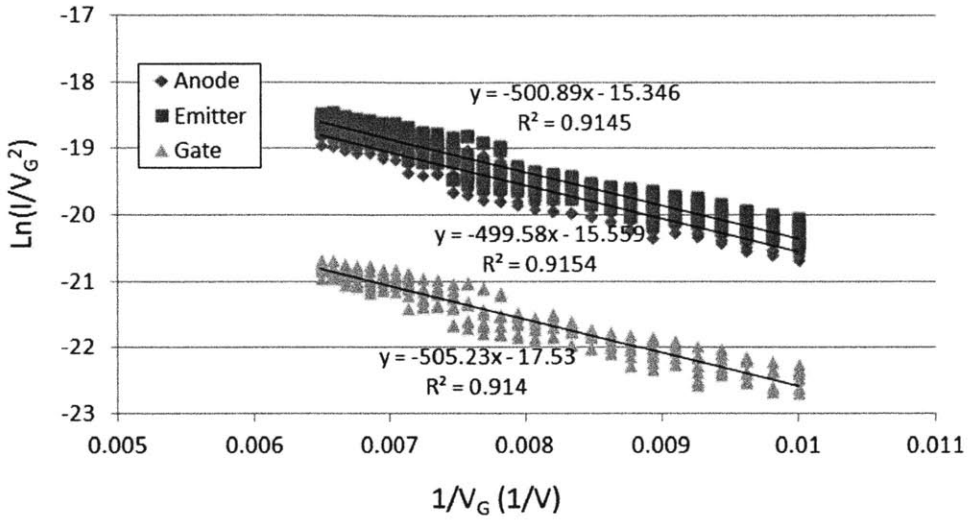

Figure 29: Fowler Nordheim Plot.

Using COMSOL, the structure of the tested device was built. The height of the tip was 3μm with radius of ~ 25nm, the oxide thickness is 1.5μm, the gate thickness is 0.45μm, and the gate aperture is 1μm. Referring to Figure 10, the simulated field factor for those paramaters is 1.08×10^6 V/cm, which is comparable to the experimental result.

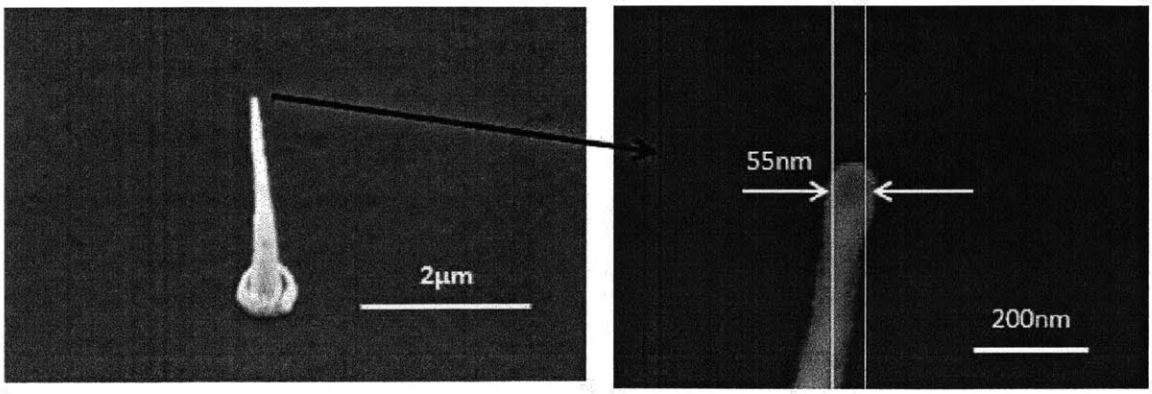

Figure 30: SEM of ~25nm carbon nanotube tip radius.

5.3 Four-terminal Measurements

The performance of the double-gated FEAs cannot be estimated using the same approach we outlined for single-gated FEAs if the gate and focus voltages are independent (if the voltages are identical, then the effective field factor $\beta = \beta_G + \beta_F$ and β can be estimated using the framework we used for single-gated FEAs). The extractor gate field factor β_G and focus gate field factor β_F are calculated from data collected by keeping fixed the focus voltage while varying the gate voltage and repeating the procedure for a different focus voltage. The least-square method is still used to obtain the estimates of the field factors, although the data processing is more elaborated. In the four-terminal measurements, the focus gate is biased at lower voltage than the extractor gate in order to collimate the electron beam. As in the single-gated FEA case, the experimental field factors are compared to the simulated result using the same geometry that is determined from SEM metrology.

We were not able to collect data in the four-terminal measurements. The double-gated FEAs were fabricated; however, the fabricated devices had two problems:

1. The fabricated focus gate was very close to the extractor gate (Figure 31) so the two gates were shorted during testing (i.e. acting as single-gated FEAs).
2. The extractor gate is shorted to the substrate (emitter tip) due to damage to the α-Si film layer on the extractor gate electrode after going through double-gated VA CNTs FEA processing (Figure 32).

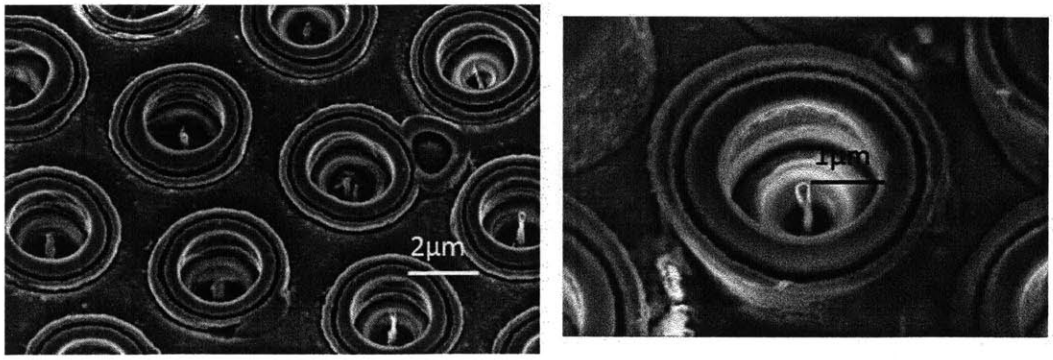

Figure 31: Double-gated FEA with focus gate position very close to the extractor gate.

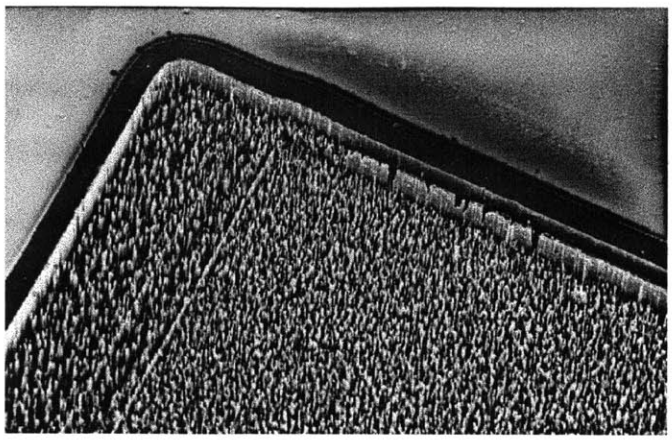

Figure 32: The damaged α-Si film layer (extractor gate electrode) looking from via. This causes the extractor gate short to the substrate during test probing.

5.4 Discussion of Literature on FEAs as electron source

There are many reports on field emission electron sources in the literature. Some of them use carbon nanotubes, carbon nanofibers, or other materials such as silicon and tungsten as sharp tips. As a comparison to our VA-CNT FEA, Table 3 shows the list of other reports using CNTs or other materials:

Table 3: Single-gated field emission array comparison using materials such as CNTs, carbon nanofiber, silicon and tungsten.

Author	Max Current	Cathode Area	Current Density	Emitter Type
Wei et al [35]	5mA	$0.79mm^2$	$1.76A/cm^2$	CNT forest with 15nm tip radii
Park et al [36]	3.67mA	$0.5mm^2$	$0.75A/cm^2$	Carbon nanofiber with Ni Catalyst
Guillorn et al [37]	-	-	5μA/tip	VA-carbon nanofiber with 30nm tip diameter
Takalkar et al [38]	2mA	$1cm^2$	-	Edge-shaped diamond FEA
Qi et al [39]	5.88mA	$1mm^2$	2.3μA/tip	Spindt-type FEA
This work	4mA	$0.8mm^2$	$0.5A/cm^2$	VA-CNTs with 50nm tip radii

This work compares well to other reports on field emission electron sources. Our device turn-on voltage is at < 80V and the current emitted from < 0.8mm^2 active area of single-gated individual FEAs biased at 200V is 4mA, compared to Wei et al's CNT forest array that emitted 5mA biased at > 1000V [35]. Our device is an array of isolated multiwall CNTs (tip radius of 25nm) with a pitch of 5μm and a height of 3-4μm in average whereas Park et al used 2μm height of carbon nanofibers (tip radius of 15nm) with a pitch of 50μm [36]. Moreover, the device structure is unique where the extractor gate is integrated to the field emitter (carbon nanotubes) in the substrate whereas most of other reports were using separate anode. In addition, the structure of carbon nanotube field emitters has excellent emission characteristics such as low average magnitude of the threshold emission field, high current density, and high emission stability, compared to other materials such as Silicon [38]. These remarkable properties make carbon nanotubes appealing as cold cathode electron sources.

6. Electron Impact Ionization Characterization

6.1 Ionization Test Set up

After benchmarking the performance of the single-gated FEAs as electron sources, we were not able to characterize them as electron impact ionizers because we damaged our devices while characterizing them as electron sources; while testing our device for field emission, most CNT tips were burnt due to a spike in the current or a breakdown in oxide layer. However, for completeness, a procedure to conduct electron-impact-ionization tests is presented; a schematic of the setup is shown in Figure 33. The pressure would be measured using a Bayard-Alpert gage from Varian, Inc connected directly to the chamber. This pressure gauge is capable of measuring a pressure between $5x10^{-10}$ and $3x10^{-2}$ Torr. The electrical set up for electron impact ionization test should be similar to the field emission test. However, instead of biasing +1100V to the anode, a voltage of -1100V would be applied in order to attract the ions produced during ionization process. A voltage of about +100V would be applied to the mesh that maximizes the electron impact ionization cross-section. The mesh attracts the electron transmitted by the extractor gate and then the electron collides with the neutral gas molecules, which results in ionization by fragmentation. By varying the background pressure in the chamber from 10^{-2} to 10^{-6} Torr, electron and ion current data would be collected at a constant pressure. From the collected data, we would be able to show that the electron impact ionization model describes the ionization process, that is, there is a linear relationship between the chamber pressure and the ratio between the ion current to electron current as predicted by Equation 9.

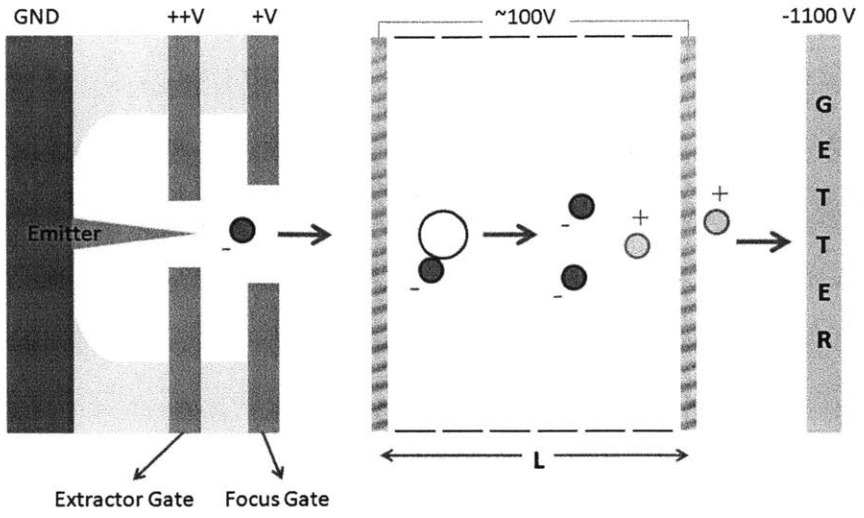

Figure 33: Field-emission electron-impact-ionization pump schematic.

6.2 Electron Impact Ionization Measurements

In order to show electron impact ionization, various ion current (I_i) versus emitter voltage across a pressure range would be collected as illustrated in Figure 34. The IV characteristics should be parallel curves, as expected from the linear dependence of the ion current on the gas pressure. At a constant electron current (constant FE operating voltage), a graph of ionization efficiency, i.e. ion-current-to-electron-current ratio, vs. pressure characteristics would be plotted (Figure 35) and should show that the data follows electron impact ionization model where the electron current to ion current ratio is linearly related to the chamber pressure [18].

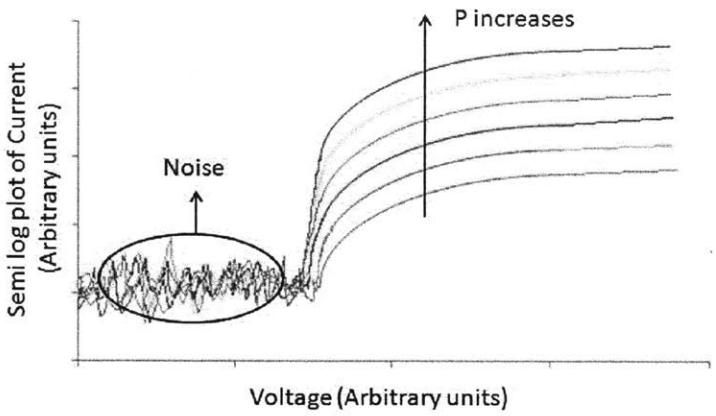

Figure 34: Illustration of ion-current versus extractor-to-emitter voltage with field emission data similar to Figure 27 at various pressure levels.

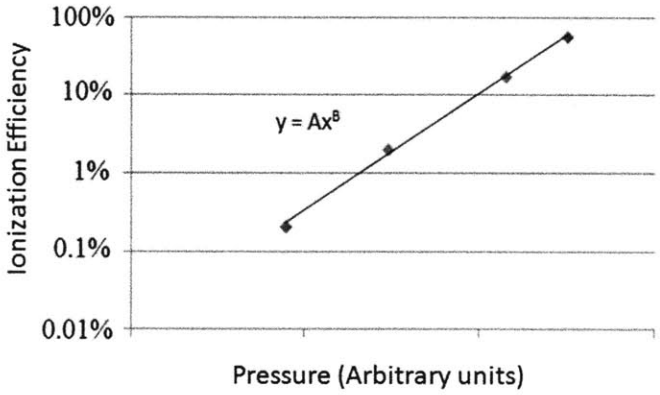

Figure 35: Log-log plot of ion-current-to-electron-current ratio versus pressure of the data at a constant operating voltage shown in Figure 34.

The power coefficient of the equation (B) should be ~1. In addition, from the coefficient of the fitted equation (A), we could calculate the average total ionization cross section, which should fall within the range of total ionization cross sections for the range of voltages that are present in the ionization region for Argon [40] by knowing the length of the ionization region (L). For further details, the reader should check the work of Chen et al [41] or the work of Velásquez-García et al [18].

A microfabricated CNT electron impact ionizer is feasible, as other researchers have demonstrated. For example, Bower et al reported a study on CNT electron impact ionization for different gasses (He, Ar, and Xe) as a function of field emission current and pressure (10^{-4} to 10^{-1} Torr). The electron-impact ion source is capable of generating ion current in excess of 1μA [11]. Also, Hwang et all reported a micro mass spectrometer that utilizes the field emission (carbon nanostructure grown on a nickel catalyst layer) current to generate ions (ionized by the laser ionization method) [42]. In addition, our group has demonstrated several generations of electron impact ionizers [13][18].

7. FEEII Pump Characterization

7.1 Pump Test Set up

Due to the lack of working devices, we were not able to conduct pump experiments. However, for completeness, the procedure on how to characterize the pump is presented in this chapter. A schematic of the setup is shown in Figure 36. The testing setup for the pump experiments would be very similar to the setup to characterize the devices as electron impact ionizers, although the pump setup has a piece of Si or Si coated with Al as getter. The electrical connections are described in Figure 36, with the getter biased at -1100V and +100V would be applied to the mesh that maximizes the FEEII cross section. The initial pressure inside the mini chamber would be set at 10^{-3} Torr, which should be the pressure after the field ionization pump stops working and electron-impact-ionization pump starts to work. Initially, a leakage characterization would be conducted by monitoring the pressure inside the mini chamber for few hours without turning on the cathode. After leakage data is collected and set the mini chamber pressure back to 10^{-3} Torr, the FEA would be turned on at a constant current for hours to observe the pressure variation inside the chamber over time. Next, the experimental data (Pressure vs. time) would be collected and analyzed and compared to the predicted model, simulated using MATLAB under the same conditions.

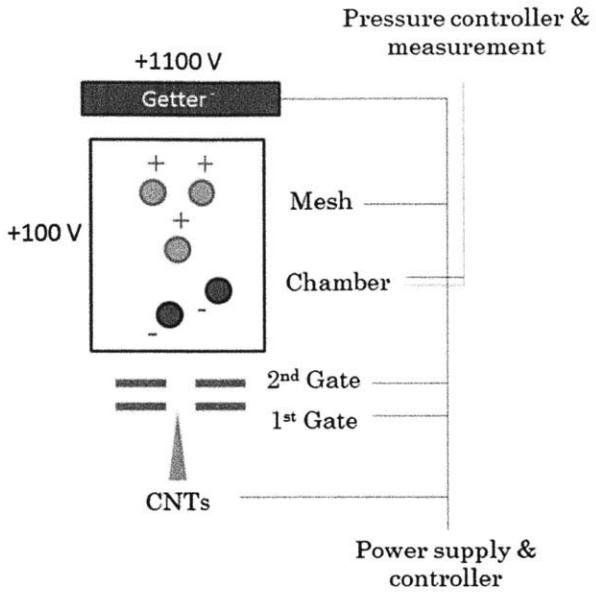

Figure 36: Field-emission electron-impact-ionization pump electrical test setup.

7.2 Pressure Measurements

To characterize the pump, pressure vs. time graph illustrated in Figure 37 and Figure 38 would be collected by applying ground to the emitter, a constant voltage to the extractor gate and focus gate where the focus gate biased at lower voltage than the extractor gate in order to protect the tip from ion bombardment and to collimate the emitted electron, +100V to the mesh, and -1100V to the getter.

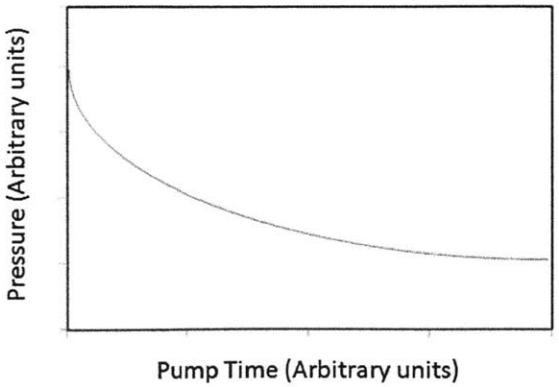

Figure 37: A conceptual sketch of Pressure vs. time if the pump rate overcomes the leak rate.

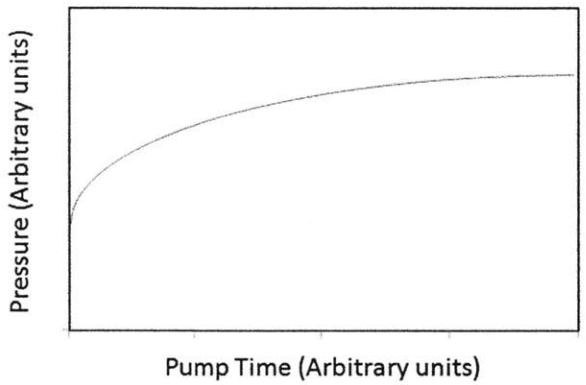

Figure 38: A conceptual sketch of Pressure vs. time if the pump cannot keep up with the leak rate. The final pressure reaches 1atm after a long period of time.

For the case in Figure 37 where the pump would successfully evacuate the chamber to lower pressure, we would calculate the characteristic time of the system (τ) by taking the log of the rate of change of pressure over time as follows:

$$\ln\left[-\frac{dP}{dt}\right] = \ln\left[\frac{P_o - P_f}{\tau}\right] - t/\tau \qquad (16)$$

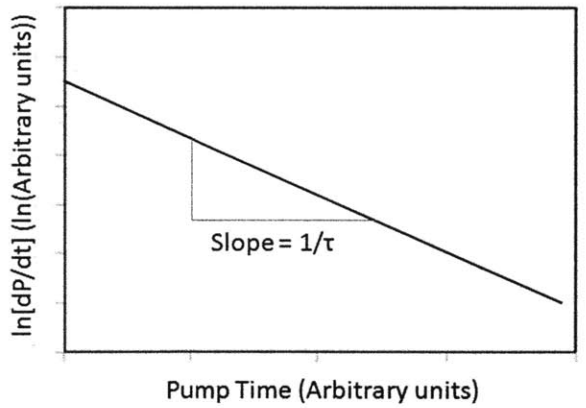

Figure 39: A conceptual sketch of ln of the rate of change of Pressure vs. time.

The slope of the graph ($1/\tau$), illustrated in Figure 38, can be compared to the characteristic time τ of our model. The ultimate pressure characterization from the experiment data could then be compared to the simulation result by MATLAB using the experimental set up parameters (chamber volume, leak rate, etc). If the pump speed is faster than the leak rate, the ultimate pressure inside the chamber settles to $P = \tau \cdot$

$\dot{N}_{lk} \cdot K_b \cdot T$ over period time as illustrated in Figure 37. On the other hand, if the leak rate is larger than the pump capacity, over a long period of time, the pressure inside the chamber rises up to atmospheric pressure (760 Torr) as illustrated in Figure 38.

8. Thesis Summary and Suggested Future Work

8.1 Thesis Summary

This thesis reports a micro scale ion pump architecture that uses an array of double-gated vertically aligned carbon nanotubes as the electron source, a high transparency mesh as the ionization region where the electron collides with the neutral gas molecules, and a solid getter that is used to implant the ions and create vacuum.

A complete fabrication procedure of double-gated vertically aligned CNTs was presented. Arrays of single multiwall CNTs with good uniformity across were successfully fabricated. Catalyst nanodots 200-300μm wide were patterned using a combination of plasma etching and wet etch (Ni etchant), which is fast, controllable, and reproducible. Then, PECVD VA-CNTs was grown from the Ni catalyst. CNTs with 3-4μm height and 25-45nm tip radius were used as the field emitters.

The opening of the extractor gate and focus gate was conducted in two ways. The first way is by polishing both extractor and focus gates up to the emitter tip, which is a self-aligned technique. However, this technique requires a 3.5μm minimum tall and uniform CNTs. The second way is by opening the extractor gate using a polishing technique and opening the focus gate using photolithography and plasma etching. This technique is better because the size of the gate aperture can be controlled and also does not depend on the deposited oxide thickness, whereas the gate aperture size in the first method is determined by the deposited oxide thickness. However, the second technique has an alignment error that needs to be improved.

Field emission test with three-terminal measurements were conducted. A single-gated FEA where the CNT height is 3μm, tip radius is 25nm, gate insulator oxide thickness is 1.5μm, gate thickness is 0.45μm, and gate aperture is 1μm was used as the electron source. The emitted current per tip produced was ~0.1μA, which is comparable to the results that Bonard et al [33] and Guillorn et al [34] reported. Extracted from the Fowler-Nordheim plot, a field factor of 1.35×10^{6} [cm^{-1}] was measured, which is

comparable to the COMSOL simulation result ($1.08x10^6$ V/cm) using the same geometry determined from SEM metrology.

8.2 Suggested Future Work

Successful field emission with single-gated VA-CNTs FEA was conducted; though, electron-impact-ionization and pump tests are left as future work. Some improvement on the fabrication of field emitter array should be explored in depth such as making the gate aperture smaller to lower the turn-on voltage and increase the emitting current. An electron-impact-ionization and pump tests for different types of gases at different pressure levels will need to be conducted to compare the performance of the ionization and getter capacity to the simulation results. The procedure on how to conduct electron-impact-ionization test is described in section 6 while section 7 presents the procedure for pumping characterization.

Leakage test of the pump test rig will need to be performed to explore the influence on the pump test and determine the leakage sources such as outgassing, internal chamber leaking, or effects from the pressure gauge in pumping the chamber. The getter performance such as capacity and the effect of ion's mass for different gasses on implantation probability should also be characterized. Therefore, the getter material selection and design is important to be explored.

Once the field emission electron-impact-ionization pump is fully characterized, the integration with the field ionization pump and two-stage mechanical pump will need to be done. The integrated performance with exploration on various methods of encapsulation and robust integration methods will need to be characterized.

Appendix A: Process Flow of the Fabrication of Double-gated vertically aligned CNT Field Emission Array

Step #	Lab	Machine	Recipe	Description
1	ICL	Coater track 1	90C 60sec	Coat 1um positive PR, prebake
2	ICL	I-stepper	120msec	Exposure, Mask #1: Alignment Mark
3	ICL	Coater track 2	Post bake 130C, 60sec	Develop, rinse + dry, post bake
4	ICL	AME5000	Pressure of 200mTorr and Cl2 of 20sccm and HBR of 20sccm	Etch 150nm deep Si
5	ICL	Asher		Remove residual resist
6	ICL	Premetal-Piranha	1:3 H2O2:H2SO4 50:1 DI:HF	Clean native oxide
7	ICL	Endura		Deposit 50nm of TiN
8	ICL	RTA	800C 30s	Anneal TiN film
9	ICL	Ebeam CMOS	Ni recipe	Deposit 20nm of Ni
10	ICL	Coater track 1	90C 60sec	Coat 1um positive PR, prebake
11	ICL	I-stepper	110msec	Exposure, Mask #2: 0.6um Nanodot
12	ICL	Coater track 2	Post bake 130C, 60sec	Develop, rinse + dry, post bake
13	ICL	Rainbow	25mTorr, 140watt RF, 10sccm of Cl2 and 40sccm of Ar	Etch Ni (pattern the dot)
14	ICL	Rainbow	13mTorr, 120watt RF, 40sccm of BCl3 and 60sccm of Cl2	Etch TiN
15	TRL	Acid hood	Ni etchant, ~20-30sec	Wet etch Ni (for smaller dot)
16	ICL	Asher		Remove residual resist
17	TRL	CCNT	770C 20 mins	Grow 3.5-4um vertically aligned CNTs
18	TRL	STSCVD	LFSIO 20mins	Deposit 1.6um of Oxide
19	TRL	STSCVD	DopedSi 15 mins	Deposit 0.45um of doped a-Silicon
20	TRL	HMDS	Recipe #5	
21	TRL	Coater	10sec 200rpm 12sec 750rpm 30sec 3krpm	Coat 1um positive PR
22	TRL	Prebake oven	95C 15mins	
23	TRL	Coater	10sec 200rpm 12sec 750rpm 30sec 3krpm	Coat another 1um positive PR

24	TRL	Prebake oven	95C 15mins	
25	TRL	EV1	7sec	Exposure, Contact mask #1: First gate contact pad
26	TRL	Developer	1min	Develop, rinse + dry
27	TRL	Post bake oven	95C 30mins	
28	TRL	STS1	Nitride 5mins	Etch a-Silicon (first gate contact pad)
29	TRL	Asher		Remove residual resist
30	ICL	GnP		Polish a-Si + oxide (open first gate)
31	ICL	Post CMP clean		
32	TRL	STSCVD	LFSIO 15mins	Deposit 1.2um of Oxide
33	TRL	STSCVD	DopedSi 15 mins	Deposit 0.45um of doped a-Silicon
34	TRL	HMDS	Recipe #5	
35	TRL	Coater	10sec 200rpm 12sec 750rpm 30sec 3krpm	Coat 1um positive PR
36	TRL	Prebake oven	95C 15mins	
37	TRL	Coater	10sec 200rpm 12sec 750rpm 30sec 3krpm	Coat another 1um positive PR
38	TRL	Prebake oven	95C 15mins	
39	TRL	EV1	7sec	Exposure, Contact mask #2: Second gate contact pad
40	TRL	Developer	1min	Develop, rinse + dry
41	TRL	Post bake oven	95C 30mins	
42	TRL	STS1	Nitride 5mins	Etch a-Silicon (second gate contact pad)
43	TRL	Asher		Remove residual resist
44	TRL	HMDS	Recipe #5	
45	TRL	Coater	10sec 200rpm 12sec 750rpm 30sec 3krpm	Coat 1um positive PR
46	TRL	Prebake oven	95C 15mins	
47	TRL	Coater	10sec 200rpm 12sec 750rpm 30sec 3krpm	Coat another 1um positive PR
48	TRL	Prebake oven	95C 15mins	
49	TRL	EV1	7sec	Exposure, Contact mask #3: Via to first gate contact pad
50	TRL	Developer	1min	Develop, rinse + dry
51	TRL	Post bake oven	95C 30mins	

52	TRL	Acid hood	7:1 BOE	Etch oxide (via to the first gate contact pad)
53	TRL	Asher		Remove residual resist
54	TRL	HMDS	Recipe #5	
55	TRL	Coater	10sec 200rpm 12sec 750rpm 30sec 3krpm	Coat another 1um positive PR
56	TRL	Prebake oven	95C 15mins	
57	ICL	I-stepper	200msec	Exposure, Mask #3: 2.5um Aperture
58	TRL	Developer	~30sec	Developer, rinse + dry
59	TRL	Post bake oven	95C 30mins	
60	TRL	STS3	Guerrertst 5mins	Etch a-Silicon (open the second gate)
61	TRL	Asher		Remove residual resist
62	TRL	Acid hood	7:1 BOE	Wet etch oxide (until the CNT tip comes out)

Appendix B: Mask Layouts

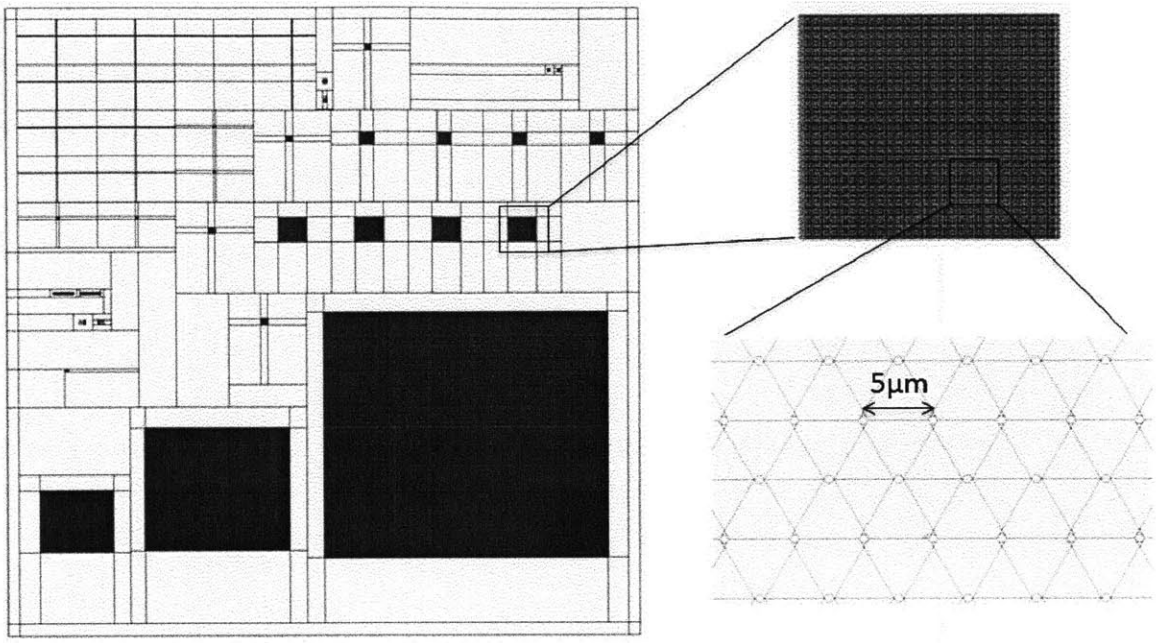

Figure B.1: Mask Layout of field emitter array of 0.6µm nanodots.

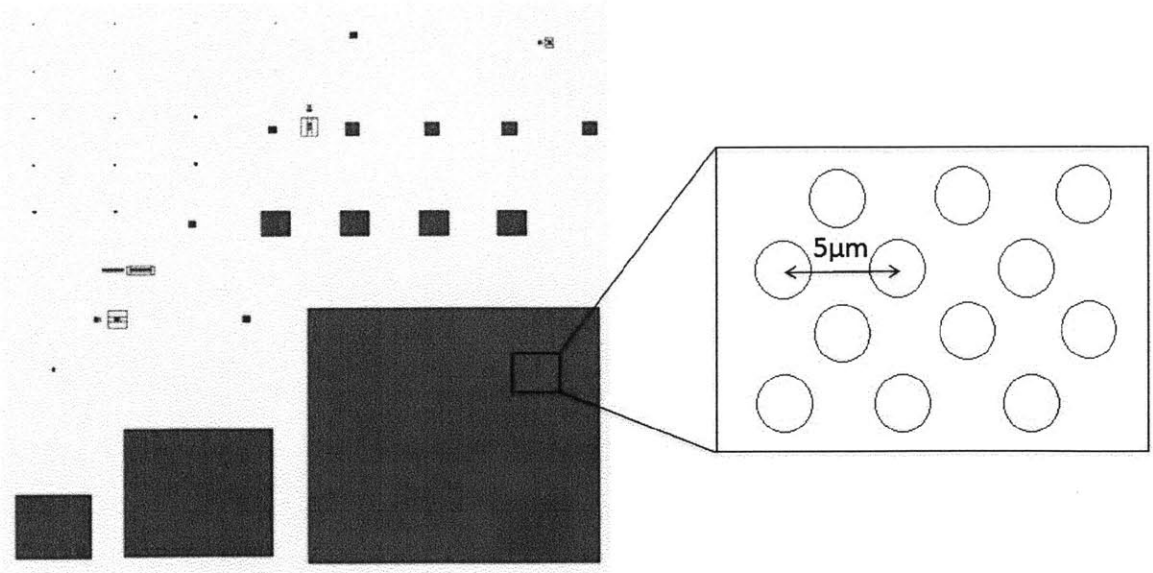

Figure B.2: Mask Layout of field emitter array of 2.5µm apertures.

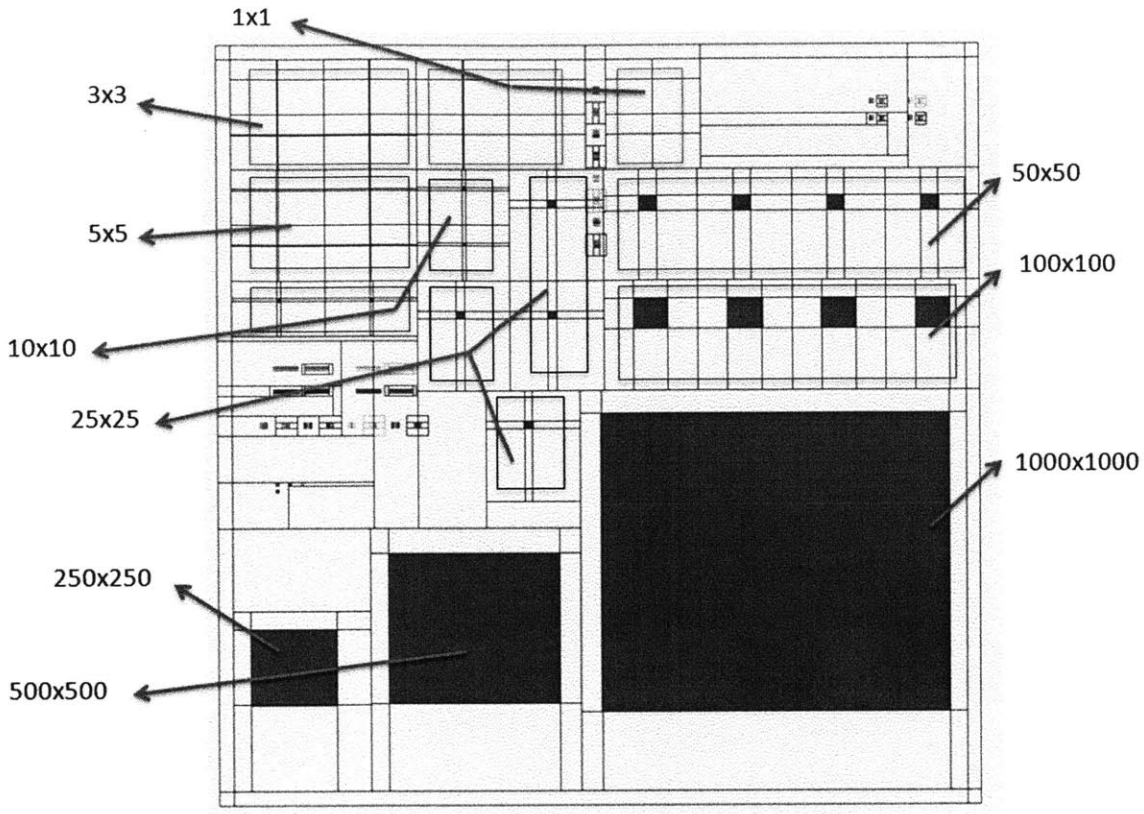

Figure B.3: Mask Layout of different array sizes.

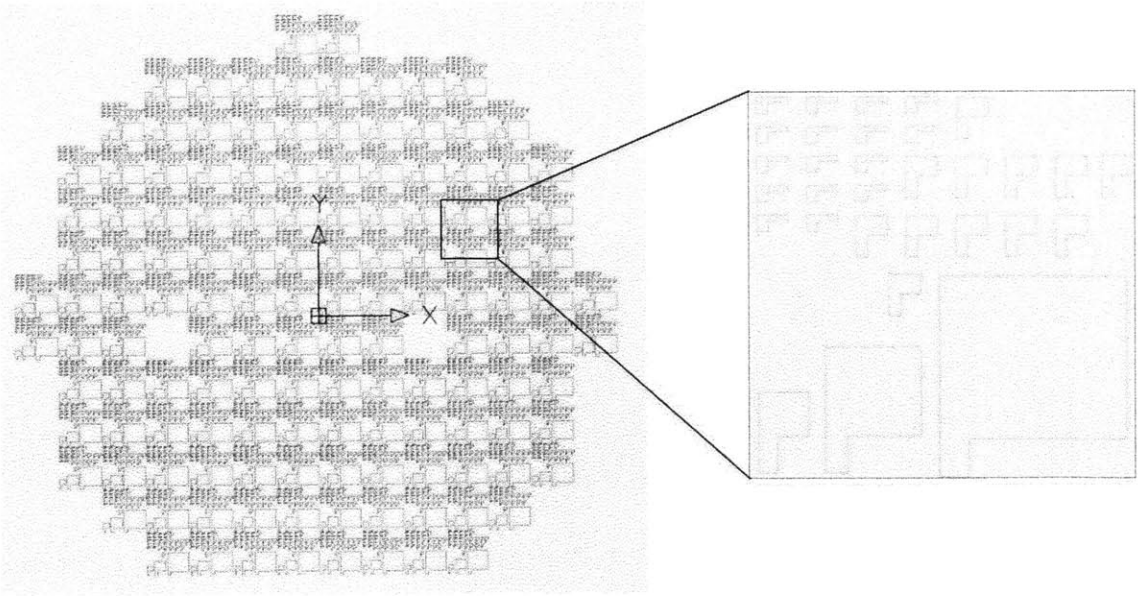

Figure B.4: Contact Mask of extractor gate electrode.

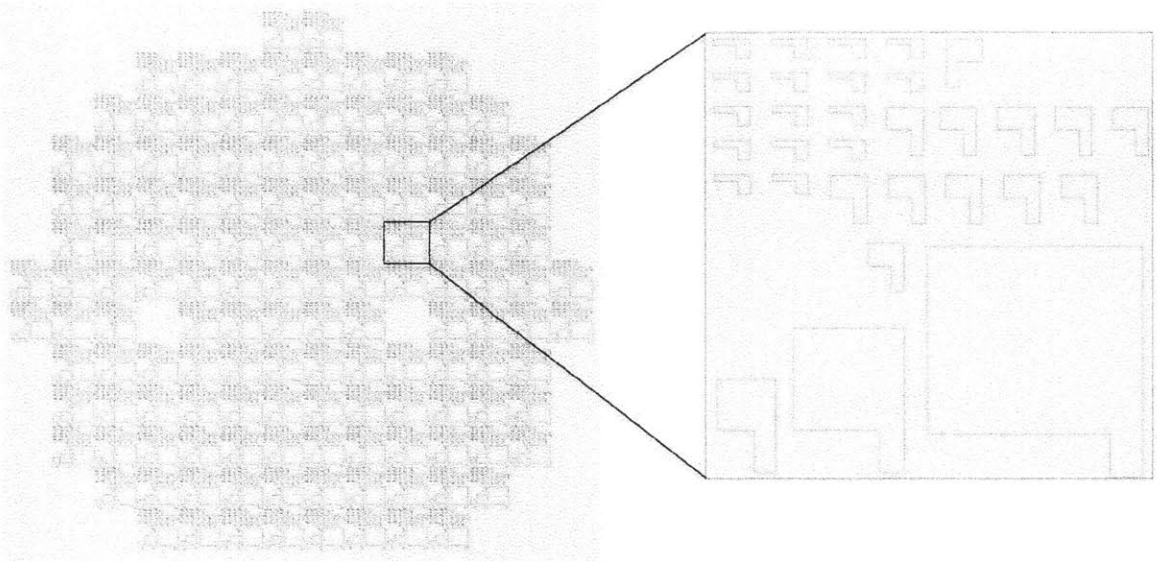

Figure B.5: Contact Mask of focus gate electrode (the orientation of the electrode is the opposite of extractor gate electrode).

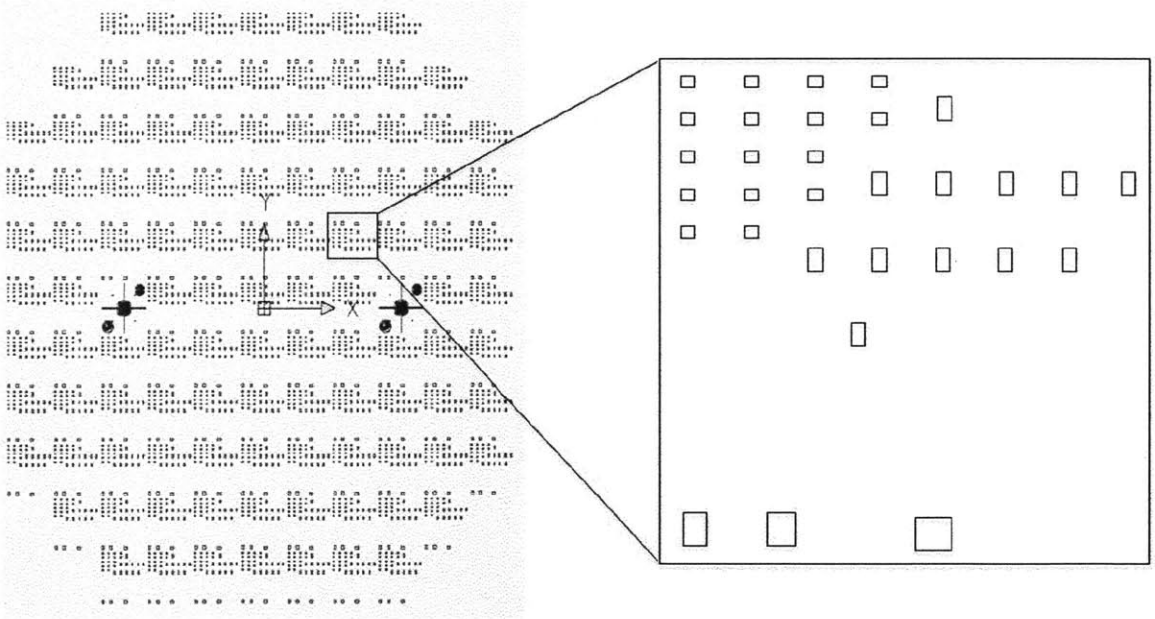

Figure B.6: Via to the extractor gate electrode.

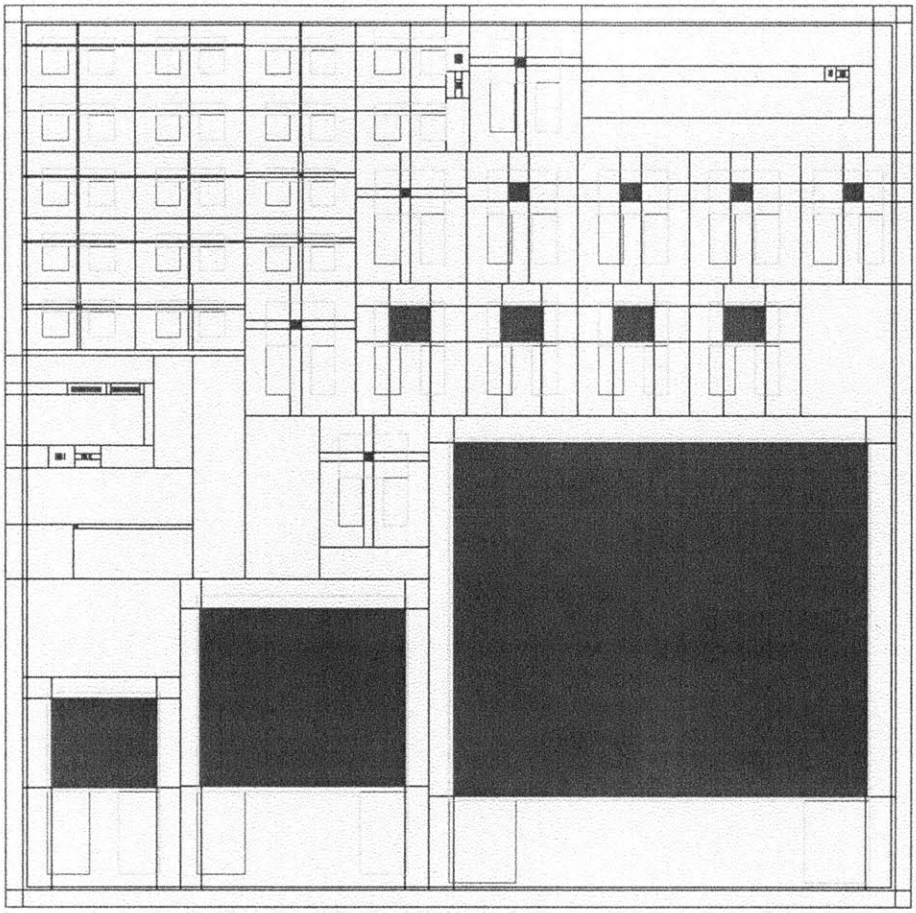

Figure B.7: Mask Layout of Nanodots + extractor and focus gate electrode.

Appendix C: Vertical and Horizontal Measurement of Deposited Oxide Thickness

I conducted an experiment to determine the relationship between vertical (H) and horizontal (W) thickness of deposited oxide as illustrated in the following figure. The result is presented in Figure C.2.

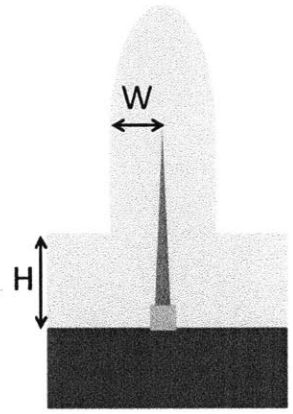

Figure C.1: Structure of a CNT emitter covered with oxide.

Vertical Oxide Thickness (μm)	Horizontal Oxide Thickness (μm)
2.5	1.88
2.15	1.62
1.48	1.15
0.89	0.66

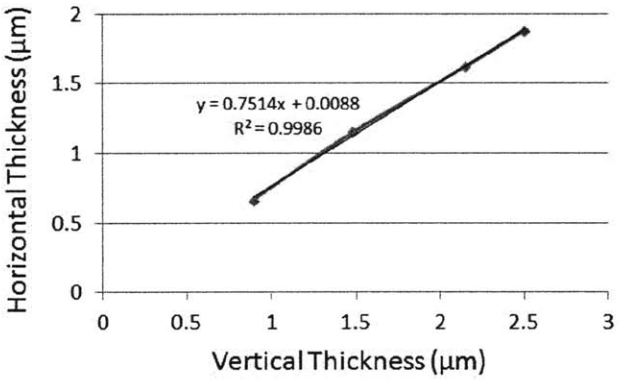

Figure C.2: Table and graph of the relationship between vertical and horizontal oxide thickness.

Figure C.2 Shows that the horizontal thickness of the deposited oxide is ~0.75 times the vertical oxide thickness. If 1μm of oxide (gate insulator) is deposited, the resulting gate aperture is 0.75μm.

Appendix D: MATLAB Scripts

PressureVsTime.m

```
function PressureVsTime

close all

% INPUT (units in MKS)
Power=1;                % Maximum Power (Watt)
Max_Current=0.1E-6;     % Maximum Current per emitter
Pitch=5;                % CNT pitch (um)
Length=3E-3;            % Length of the chamber (m)
Mech_Vol=0.3;           % Mechanical Pump volume (mm^3)
Res_Vol=0.25;           % Resonator volume (mm^3)
Con_Vol=6;              % Connectors volume (mm^3)
V_getter=1000;          % Getter Voltage
Init_P=1E-3;            % Initial Pressure (Torr)
Surf_Area=15;           % Chamber surface area (pump area is ~0.05cm^2
                          and length of chamber 4mm) in cm^2
Or=7.6E-10;             % Typical Outgassing rate (for stainless steel)
                          in Torr.L/cm^2.sec
Volume=20E-6;           % Chamber volume (m^3)

% Constants
N2sigma=1.5e-16;    % (cm^2)
O2sigma=3.1e-16;    % (cm^2)
Arsigma=3.5e-16;    % (cm^2)
q=1.6e-19;
k=1.38e-23;
Temperature=300;
t=(0:0.000001:0.003);

nOr=Or*1E-3*Surf_Area*133/(k*Temperature);  % leakage by outgassing
nleak1=1E-3*1E-9*760*133/(k*Temperature);   % leakage1
nleak2=5E-3*1E-9*760*133/(k*Temperature);   % leakage2
nleak3=0.01*1E-9*760*133/(k*Temperature);   % leakage3
nleakage1=nleak1+nOr;             % total number of molecules leakage1
nleakage2=nleak2+nOr;             % total number of molecules leakage2
nleakage3=nleak3+nOr;             % total number of molecules leakage3

% Area Needed
Peak_I=Power/V_getter;                % Peak Current
N_emitter=Peak_I/Max_Current;         % Number of Emitter
Area=N_emitter*Pitch*Pitch/1.15       % Area needed (um^2)
J=N_emitter*Max_Current*1E8/Area;     % Current density (/cm^2)

Rest_Vol=(Mech_Vol+Res_Vol+Con_Vol)*1E-9;   % volume of the rest of the
                                              system (m^3)
FEII_Vol=Length*Area*1E-12*3                % volume of feii pump (m^3)
Ion_Vol=100*1E-6*(1E-4-Area*1E-12*3);       % volume of ionization pump
                                              (m^3) with 100um length

alpha=FEII_Vol/(FEII_Vol+Ion_Vol+Rest_Vol);
```

```
n0=Init_P*133*Volume/(k*Temperature);    % Initial number of molecules

taoN2=q*alpha/(N2sigma*J);
taoO2=q*alpha/(O2sigma*J);
taoAr=q*alpha/(Arsigma*J);

nN2_1=(n0*0.78-nleakage1*taoN2)*exp(-t/taoN2)+nleakage1*taoN2;
nO2_1=(n0*0.21-nleakage1*taoO2)*exp(-t/taoO2)+nleakage1*taoO2;
nAr_1=(n0*0.01-nleakage1*taoAr)*exp(-t/taoAr)+nleakage1*taoAr;
n1=nN2_1+nO2_1+nAr_1;
Pressure1=(n1*k*Temperature/Volume)/133;

nN2_2=(n0*0.78-nleakage2*taoN2)*exp(-t/taoN2)+nleakage2*taoN2;
nO2_2=(n0*0.21-nleakage2*taoO2)*exp(-t/taoO2)+nleakage2*taoO2;
nAr_2=(n0*0.01-nleakage2*taoAr)*exp(-t/taoAr)+nleakage2*taoAr;
n2=nN2_2+nO2_2+nAr_2;
Pressure2=(n2*k*Temperature/Volume)/133;

nN2_3=(n0*0.78-nleakage3*taoN2)*exp(-t/taoN2)+nleakage3*taoN2;
nO2_3=(n0*0.21-nleakage3*taoO2)*exp(-t/taoO2)+nleakage3*taoO2;
nAr_3=(n0*0.01-nleakage3*taoAr)*exp(-t/taoAr)+nleakage3*taoAr;
n3=nN2_3+nO2_3+nAr_3;
Pressure3=(n3*k*Temperature/Volume)/133;

nN2_NoLeak=(n0*0.78)*exp(-t/taoN2);
nO2_NoLeak=(n0*0.21)*exp(-t/taoO2);
nAr_NoLeak=(n0*0.01)*exp(-t/taoAr);
n_NoLeak=nN2_NoLeak+nO2_NoLeak+nAr_NoLeak;
Pressure_NoLeak=(n_NoLeak*k*Temperature/Volume)/133;

time=t*1000;
semilogy(time,Pressure_NoLeak,'o', time, Pressure3, '+', time, Pressure2,'x',
time, Pressure1,'*');
xlabel('Pumping Time(sec)')
ylabel('Pressure (Torr)')
title('Pumping rate for the Electron Impact Ionization Pump')
grid on;
```

References

[1] C. E. Hunt, A.G. Chakhovskoi, N. N. Chubun, and M. S. Hajra, "Challenges and new applications in vacuum microelectronics", *Third IEEE International Vacuum Electronics Conference 2002.*

[2] Z. Ouyang and R. G. Cooks, "Miniature Mass Spectrometers", *Annual Review of Analytical Chemistry*, Vol. 2, pp. 187-214, Feb. 2009.

[3] American Vacuum Society, Glossary, *AVS Reference Guide*, Retrieved 2006-03-15.

[4] L. Jurong and W. Xufei, "Design and experiment of a new positive-displacement pump," *2010 International Conference on Computing, Control and Industrial Engineering*, Vol. 1, pp. 271-275, June 2010.

[5] R. Crane, "Magnetic bearings for high speed turbo molecular pumps," *IEE Colloquium on High Speed Bearings for Electrical Machines*, pp. 4/1-6, April 1997.

[6] S. McNamara, Y. B. Gianchandani, "On-chip vacuum generated by a micromachined Knudsen pump", *Journal of Microelectromechanical Systems,* Vol. 14, No. 4, pp. 741-6, Aug. 2005.

[7] R. Kersevan, Y. Li and N. B. Nariman, "Operational experience of novel vacuum chambers incorporating massive titanium-sublimation pumping in the Cornell electron-positron storage ring interaction region", *Journal of Vacuum Science and Technology,* Vol. 15, No. 3, pp. 716, May 1997.

[8] R. T. Jacobsen, S. G. Penoncello, and E. W. Lemmon, *Thermodynamic Properties of Cryogenic Fluids*, Plenum Press, New York, 1997.

[9] T. Tom, "Use of a metallic ion source in cold cathode sputter ion pumps", *Journal of Vacuum Science and Technology,* Vol. 9, No. 1, pp. 383, Jan. 1972.

[10] H. Zhou, "A study of Micromachined Displacement Pumps for Vacuum Generation", PhD Thesis, MIT, 2011.

[11] C. A. Bower, K. H. Gilchrist, J. R. Piascik, B. R. Stoner, S. Natarajan, C. B. Parker, S. D. Wolter, and J. T. Glass, "On-chip electron-impact ion source using carbon nanotube field emitters", *Applied Physics Letters,* Vol. 90, No. 12, pp. 124102, Mar. 2007.

[12] Y. Changyi, D. N. Jamieson, S. Hearne, T. Hopf, C. Pakes, S. Prawer, S. O. Andresen, A. Dzurak, E. Gauja, F. E. Hudson, R. G. Clark, "Integration of single ion implantation method in focused ion beam system for nanofabrication", *International Conference on Nanoscience and Nanotechnology,* July 2006.

[13] L. Y. Chen, "Double-gated Isolated Vertically Aligned Carbon Nanofiber Field Emission and Field Ionization Arrays", PhD Thesis MIT, Cambridge MA, 2007.

[14] W.A. de Heer, A. Chatelain, and D. Ugarte, "A carbon nanotube field-emission electron source", *Science*, Vol. 270, No. 5239, pages 1179-1180, Nov 1995.

[15] I. Ben-Zvi, "Performance of photocathode RF gun electron accelerators", *Proceedings of the 1993 article Accelerator Conference*, pp. 2962, 17-20 May 1993.

[16] E. L. Murphy and R. H. Good, "Thermionic emission, field emission, and the transition region", *Physical Review,* Vol. 102, No. 6, pp. 1464-73, 15 June 1956.

[17] R. Gomer, *Field Emission and Field Ionization,* Harvard University Press, 1961.

[18] L. F. Velásquez-García, B. Gassend, and A. I. Akinwande, "CNT-based MEMS ionizers for portable mass spectrometry applications", *Journal of Microelectromechanical Systems,* Vol. 19, No. 3, pp. 484-93, 2010.

[19] C. A. Spindt, I. Brodie, L. Humphrey, and E. R. Westerberg, "Physical properties of thin-film field emission cathodes with molybdenum cones", *Journal of Applied Physics,* Vol. 47, No. 12, pages 5248–63, Dec. 1976.

[20] L. Dvorson, G. Sha, I. Kymissis, C.-Y. Hong, and A.I. Akinwande, "Electrical and optical characterization of field emitter tips with integrated vertically stacked focus", *IEEE Trans. Electron Devices,* Vol. 50, No. 12, pages 2548–58, Dec. 2003.

[21] L. J. Kieffer and G. H. Dunn, "Electron impact ionization cross-section data for atoms, atomic ions, and diatomic molecules: I. Experimental data," *Rev. Mod. Phys.,* Vol. 38, No. 1, pp. 1–35, Jan. 1966.

[22] C. J. Gasdaska, P. Falkos, V. Hruby, M. Robin, N. Demmons, R. McCormick, D. Spence, and J. Young, "Testing of carbon nanotube field emission cathodes," *40th AIAA/ASME/SAE/ASEE Joint Propulsion Conf. and Exhibit*, Fort Lauderdale, FL, Jul. 11–14, 2004, Paper AIAA 2004-3427.

[23] G. Lewin, *Fundamentals of Vacuum Science and Technology*, McGraw Hill Inc., 1965.

[24] P.A. Redhead, J.P. Hobson, and E.V. Kornelsen, *The physical Bases of Ultra High Vacuum*, Chapman and Hall Ltd., 1968.

[25] R.C. Smith, W.M. Tsang, D.C. Cox, and S.R.P. Silva, "Electron field emission from a single carbon nanotube: effects of anode location," *Technical Digest of the 18th International Vacuum Nanoelectronics Conference, 2005*, pp. 264-265, July 2005.

[26] D.L. Niemann, B.P. Ribaya, N. Gunther, J. Leung, M. Rahman, and C.V. Nguyen "Computational modeling of field enhancement in an individual carbon nanotube field emitter system," *Vacuum Electronics Conference*, pages 509-510, April 2009.

[27] L. Thien-Nga, J-M. Bonard, R. Gaal, L. Forro, K. Hernadi, "Comparison of catalytically grown and arc-discharge carbon nanotube tips," *Applied Physics Letters*, Vol. 80, No. 5, pages 850-852, Feb. 2002.

[28] *NASA's Outgassing Data Table*, available at http://outgassing.nasa.gov/.

[29] S.C. Sun, M.H.Tsai, "Effect of rapid thermal annealing of the electrical and physical properties of metalorganic chemical-vapor-deposited TiN," *Appl. Phys. Lett.* 68 (5), Nov 1995.

[30] H.N. Cho, R.M. Su, H.J. Bae, J.H. Lee, and C.W. Chung, "High density plasma etching of nickel thin films using a Cl2/Ar plasma," *J. Ind. Eng. Chem.*, Vol. 13, No. 6, pages 939-943, July 2007.

[31] K.B.K. Teo, M. Chhowalla, G.A.J. Amaratunga, W.I. Milne, D.G. Hasko, G. Pirio, P. Legagneux, F. Wyczisk, and D. Pribat, "Uniform patterned growth of carbon nanotubes without surface carbon," *Applied Physics Letters*, Vol. 79, No. 10, pages 1534-1536, Sept. 2001.

[32] K. Kim, Y.Song, G.S. Lee, and J. Song, "Electrical properties of PECVD oxide films deposited at room temperature," *Electronics Letters*, Vol. 32, No. 21, pages 2015-2016, Oct 1996.

[33] J.M. Bonard, F. Maier, T. Stokli, A. Chaelain, W.A. de Heer, J.-P. Salvetat, and L. Forr, "Field emission properties of multiwalled carbon nanotubes," *Ultramicroscopy*, Vol. 73, No. 1-4, pp.7-15, June 1998.

[34] M.A. Guillorn, A.V. Melechko, V.I. Merkulov, E.D. Ellis, C.L. Britton, M.L. Simpson, D.H. Lowndes, and L.R. Baylor, "Operation of a gated field emitter using an individual carbon nanofiber cathode," *Applied Physics Letters*, Vol. 79, No. 21, pages 3506-3508, Nov 2001.

[35] L. Wei, Z. Xiaobing, C. Jing, Z. Zhiwei, C. Yiping, and W. Baoping, "Very high field emission from a carbon nanotube array with isolated subregions and balanced resistances," *IEEE Transactions on Electron Devices*, Vol. 58, No. 10, pages 3616-3621, Oct. 2011.

[36] K.H. Park, J.H. Yim, S. Lee, and K.H. Koh, "High current field emission from carbon nanofiber films grown using electroplated Ni catalyst," *Microelectronics and Nanometer Structures: Journal of Vacuum Science & Technology B*, Vol. 23, No. 2, pages 776-780, March 2005.

[37] M.A. Guillorn, A.V. Melechko, V.I. Merkulov, E.D. Ellis, M.L. Simpson, D.H. Lowndes, L.R. Baylor, and G.J. Bordonaro, "Microfrabricated field emission devices using carbon nanofibers as cathode elements," *Microelectronics and Nanometer Structures: Journal of Vacuum Science & Technology B*, Vol. 19, No. 6, pages 2598-2601, Nov 2001.

[38] R.S. Takalkar, J.L. Davidson, W.P. Kang, A. Wisitsora-at, and D.V. Kerns, "Edge-shaped diamond field emission arrays," *Technical Digest of the 17th International Vacuum Nanoelectronics Conference*, pages156-157, July 2004.

[39] K.C. Qi, Z.L. Lin, W.B. Chen, G.C. Cao, J.B. Cheng, and X.W. Sun, "Formation of extremely high current density LaB6 field emission array via e-beam deposition," *Applied Physics Letters*, Vol. 93, No. 9, pages 093503-093503-3, Sept 2008.

[40] H.C. Straub, P. Renault, B.G. Lindsay, K.A. Smith, and R.F. Stebbings, "Absolute partial and total cross sections for electron-impact ionization of argon from threshold to 1000eV," *Phys. Rev. A*, Vol. 52, pages 1115-1124, 1995.

[41] L.Y. Chen, L.F. Velasquez-Garcia, W. Xiazhi, K. Teo, and A.I. Akinwande, "A microionizer for portable mass spectrometers using double-gated isolated vertically aligned carbon nanofiber arrays," *IEEE Transactions on Electron Devices*, Vol. 58, No. 7, pages 2149-2158, July 2011.

[42] J.S. Hwang, S.W. Park, J.B. Cho, K.S. Oh, S.S. Yang, L. Soonil, K.H. Koh, and K.W. Jung, "The micro mass spectrometer with a carbon nano structure ion source," *1st IEEE International Conference on Nano/Micro Engineered and Molecular Systems*, pages 1220-1223, Jan. 2006.